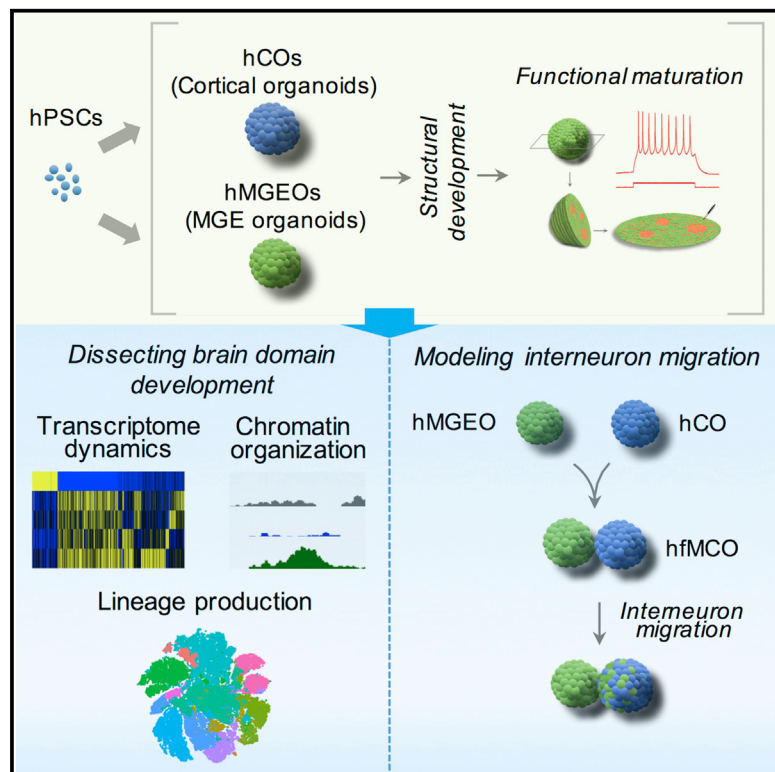


Fusion of Regionally Specified hPSC-Derived Organoids Models Human Brain Development and Interneuron Migration

Graphical Abstract



Authors

Yangfei Xiang, Yoshiaki Tanaka,
Benjamin Patterson, ..., Sang-Hun Lee,
Sherman M. Weissman, In-Hyun Park

Correspondence

inhyun.park@yale.edu

In Brief

Xiang and colleagues report a method for generating human medial ganglionic eminence (MGE)-like organoids (hMGEos) and cortical-like organoids (hCOs), which resemble the developing human MGE and cortex, respectively. By fusing hMGEos and hCOs, they establish a 3D model to investigate human interneuron migration.

Highlights

- hMGEos and hCOs recapitulate human brain organization and fetal brain transcriptomes
- Transcriptome and chromatin accessibility distinguish hMGEos and hCOs
- hMGEos and hCOs display activity-dependent and synchronized calcium oscillations
- Interneurons migrate from hMGEos and functionally integrate in hCOs

Fusion of Regionally Specified hPSC-Derived Organoids Models Human Brain Development and Interneuron Migration

Yangfei Xiang,^{1,8} Yoshiaki Tanaka,^{1,8} Benjamin Patterson,¹ Young-Jin Kang,² Gubbi Govindaiah,² Naomi Roselaar,¹ Bilal Cakir,¹ Kun-Yong Kim,¹ Adam P. Lombroso,³ Sung-Min Hwang,¹ Mei Zhong,⁴ Edouard G. Stanley,^{5,6,7} Andrew G. Elefanty,^{5,6,7} Janice R. Naegle,³ Sang-Hun Lee,² Sherman M. Weissman,¹ and In-Hyun Park^{1,9,*}

¹Department of Genetics, Yale Stem Cell Center, Yale School of Medicine, New Haven, CT 06520, USA

²Department of Neurology, University of Arkansas for Medical Sciences, Little Rock, AR 72205, USA

³Department of Biology, Program in Neuroscience and Behavior, Hall-Atwater Laboratory, Wesleyan University, Middletown, CT 06459, USA

⁴Department of Cell Biology, Yale Stem Cell Center, Yale School of Medicine, New Haven, CT 06520, USA

⁵Murdoch Childrens Research Institute, The Royal Children's Hospital, Parkville, VIC 3052, Australia

⁶Department of Paediatrics, Faculty of Medicine, Dentistry and Health Sciences, University of Melbourne, Parkville, VIC 3052, Australia

⁷Department of Anatomy and Developmental Biology, Faculty of Medicine, Nursing and Health Sciences, Monash University, Clayton, VIC 3800, Australia

⁸These authors contributed equally

⁹Lead Contact

*Correspondence: inhyun.park@yale.edu

<http://dx.doi.org/10.1016/j.stem.2017.07.007>

SUMMARY

Organoid techniques provide unique platforms to model brain development and neurological disorders. Whereas several methods for recapitulating corticogenesis have been described, a system modeling human medial ganglionic eminence (MGE) development, a critical ventral brain domain producing cortical interneurons and related lineages, has been lacking until recently. Here, we describe the generation of MGE and cortex-specific organoids from human pluripotent stem cells that recapitulate the development of MGE and cortex domains, respectively. Population and single-cell RNA sequencing (RNA-seq) profiling combined with bulk assay for transposase-accessible chromatin with high-throughput sequencing (ATAC-seq) analyses revealed transcriptional and chromatin accessibility dynamics and lineage relationships during MGE and cortical organoid development. Furthermore, MGE and cortical organoids generated physiologically functional neurons and neuronal networks. Finally, fusing region-specific organoids followed by live imaging enabled analysis of human interneuron migration and integration. Together, our study provides a platform for generating domain-specific brain organoids and modeling human interneuron migration and offers deeper insight into molecular dynamics during human brain development.

INTRODUCTION

Self-renewing and pluripotency features of human pluripotent stem cells (hPSCs) have greatly facilitated understanding of the

developing human nervous system and the pathogenesis of various neurological disorders (Mertens et al., 2016). Since the first report of neural rosette formation from human embryonic stem cells (ESCs) (Zhang et al., 2001), techniques to derive neural cells from hPSCs have continuously evolved such that now we readily generate neural tissues *in vitro* that resemble the three-dimensional (3D) organization of various brain regions (Kelava and Lancaster, 2016; Lancaster and Knoblich, 2014). Compared with monolayer cultures, 3D neural tissues, named as brain organoids, provide unique opportunities to study neural development and to model neurological disorders (Quadrato et al., 2016). Recent studies identified human-cell-type-specific phenotypic changes during corticogenesis using brain organoid systems (Bershteyn et al., 2017; Li et al., 2017) and have studied the diversity of cell types generated during organoid development using large-scale single cell analysis (Quadrato et al., 2017).

Glutamatergic pyramidal neurons and GABAergic interneurons comprise cerebral cortex together with non-neuronal astrocytes and oligodendrocytes. Pyramidal neurons arise from the pallium, specifically, from radial glial cells (RGs) in the ventricular zone (VZ) and from outer radial glial cells (oRGs) and intermediate progenitors (IPs) in the subventricular zone (SVZ). In contrast, cortical interneurons are derived chiefly from the medial ganglionic eminence (MGE) of subpallium, then migrate tangentially to the cerebral cortex, and finally integrate into local neural networks (Hansen et al., 2013; Ma et al., 2013). Interneurons are critical for modulating the activity of cortical networks (Markram et al., 2004), and disruption in interneuron activity has been associated with various neurological diseases (Chao et al., 2010; Mariani et al., 2015). Realizing the critical role of interneurons in shaping brain development and in the etiology of multiple neurological disorders, methods to generate interneuron-enriched neural culture from hPSCs have been developed (Germain et al., 2013; Liu et al., 2013; Maroof et al., 2013; Nicholas et al., 2013).

To date, most studies have focused on generating brain organoids resembling cortex development (Kadoshima et al., 2013; Lancaster et al., 2013; Mariani et al., 2012; Pașca et al., 2015; Qian et al., 2016). Methods to generate organoids resembling MGE development have been recently described (Bagley et al., 2017; Birey et al., 2017); however, further study is warranted given the paucity of protocols for generating ventrally specified organoids. Moreover, cell transplantation or explant cultures have been used to model interneuron migration *in vivo* or *in vitro* (Bellion et al., 2005; Maroof et al., 2013; Nicholas et al., 2013), but these studies have largely relied upon xenografts of human cells into immunodeficient mice. To recapitulate 3D neuronal migration *in vitro*, biomaterial-based methods were recently established (Zhang et al., 2016). However, such systems still lack a physiological cellular environment, necessitating 3D culture systems to model interneuron migration in the context of human developing cortex, which have been recently reported (Bagley et al., 2017; Birey et al., 2017).

Here, we describe a 3D culture system for generating human brain organoids resembling the MGE domain (human MGE organoids [hMGEOs]) and cortical domain (human cortical organoids [hCOs]). hMGEOs and hCOs displayed cellular organizations similar with developing MGE and cortex, respectively. Cells interior of hMGEOs and hCOs efficiently developed neuronal activity. We performed transcriptome profiling utilizing developing hMGEOs and hCOs in parallel to examine their dynamics. Furthermore, genome-wide chromatin accessibility landscapes were characterized for hMGEOs and hCOs to investigate transcriptional regulation mechanism. Moreover, we profiled single-cell transcriptome of developing hMGEOs and hCOs. Finally, we describe a 3D approach to assay human interneuron migration by fusing hMGEOs with hCOs to produce human fused MGE-cortical organoids (hfMCOs).

RESULTS

Generation of hMGEOs and hCOs

We generated hMGEOs and hCOs based on the developmental principles that anterior neuroectodermal fates can be achieved by dual SMAD inhibition (Chambers et al., 2009), and activation of sonic hedgehog (SHH)-signaling pathway induces ventral fates (Maroof et al., 2013; Nicholas et al., 2013). Canonical Wnt signaling was also inhibited in order to enhance the neural induction (Maroof et al., 2013; Nicholas et al., 2013; Figure 1A; see STAR Methods for details). The MGE of developing ventricular zone in the human brain is marked by the expression of NKX2-1. To facilitate the identification of this domain, we used a previously established and widely adopted *NKX2-1-GFP* reporter hESC line (HES-3 *NKX2-1*^{GFP/w}; Germain et al., 2013; Goulburn et al., 2011; Maroof et al., 2013; Nicholas et al., 2013). We observed robust *NKX2-1-GFP* induction that marked the whole organoid by day 18 using hMGE protocol (Figure 1B). In contrast, organoids generated from hCO protocol showed a limited cluster of *NKX2-1-GFP*⁺ cells, indicating spontaneous production of MGE progenitors inside hCOs (Figure 1B). In total, we produced over 400 hMGEOs and over 300 hCOs. By day 21, 82.40% ± 5.14% (n = 10 hMGEOs; mean ± SD) of cells dissociated from hMGEOs expressed *NKX2-1-GFP*, whereas *NKX2-1-GFP*⁺ cells only account for 2.59% ± 1.17% (n = 9 hCOs;

mean ± SD) of the total cell population from hCOs (Figure 1C). At this stage, 93.97% ± 4.78% of hMGEOs cells were FOXG1 positive, and 79.85% ± 5.67% of FOXG1⁺ cells were also *NKX2-1-GFP* positive (n = 10 hMGEOs; mean ± SD; Figure 1D). Meanwhile, 94.78% ± 3.56% of cells from hCOs were PAX6 and FOXG1 double positive (Figure 1E), confirming that hCOs underwent efficient telencephalic development. However, we rarely detected PAX6⁺ cells in dissociated hMGEO culture (Figure S1A), consistent with the expression patterns of PAX6 in developing subcortical domains (Hansen et al., 2013; Ma et al., 2013). Histological analysis revealed neural rosette-like structures that resemble the proliferative regions of the human VZ in both hMGEOs and hCOs (Figure 1F). Both hMGEOs and hCOs gradually gained size when maintained in spinning culture, and after 2 months, hMGEOs and hCOs reached up to 3 mm in diameter (Figure 1G).

hMGEOs Recapitulate Human MGE Development

Newborn neurons in the ganglionic eminences are generated from RGs (neuroepithelial stem cells) in the VZ and from IPs in the SVZ. We found that radially organized cells resembling VZ in hMGEOs were enriched with SOX2-expressing cells, confirming their identity as neuroepithelial stem cells (Figure 2A). Outside the VZ-like area, there were SOX2⁺ progenitors delineating OSVZ-like area, but ISVZ-like area was distinguishable only at early stage (Figure 2A). In dissociated cultures of early hMGEOs (day 21), we found that there were three sub-populations of neural progenitors: (1) SOX2⁺/*NKX2-1-GFP*⁻ progenitors (19.76% ± 6.39%; n = 10 hMGEOs; mean ± SD); (2) SOX2⁺/*NKX2-1-GFP*⁺ progenitors (51.09% ± 7.93%; n = 10 hMGEOs; mean ± SD); and (3) SOX2⁻/*NKX2-1-GFP*⁺ progenitors (25.96% ± 5.34%; n = 10 hMGEOs; mean ± SD), which may represent different developmental stages of MGE progenitors (Figure S1B; Hansen et al., 2013). Indeed, the RG marker GFAP was only present in less-neuronally committed cells (Figure S1C). We found a marked trend toward a decrease of VZ-like area during hMGEOs development. Whereas VZ-like area at early stages consisted of over ten layers of stratified SOX2⁺ nucleus, the thicknesses of VZ-like area decreased during further development. By day 71, only three or four layers of SOX2⁺ progenitors were identifiable within the VZ-like area (Figures 2A–2C). We found that the diameter of VZ-like area decreased from an average of 59.64 ± 2.64 μm on day 22 to 38.32 ± 1.45 μm on day 44 and 30.55 ± 1.33 μm on day 71 (Figure 2D). Although the overall thickness of VZ-like area in hMGEOs was less than that in the developing human brain, the observed trend is consistent with a previous report in human fetal brain tissues (Hansen et al., 2013).

To determine whether the diminishment of VZ-like area is due to the differentiation of SOX2⁺ progenitors in this zone of the organoids, we next examined the distribution of DLX2-positive neuroblasts. In early-stage hMGEOs, whereas SOX2 expression was enriched in VZ- and OSVZ-like area, DLX2 expression was largely excluded from VZ-like area (Figure 2E). After further development, more DLX2⁺ cells were distributed in VZ-like area with decrease of width of VZ-like area (Figure 2F). Moreover, ASCL1⁺ cells were present in VZ-like area at this stage (Figure S1D). Given the critical roles of DLX2 and ASCL1 in cell fate decision during subpallial VZ and SVZ development, these results suggest that, as cells in SVZ-like area become neuronally

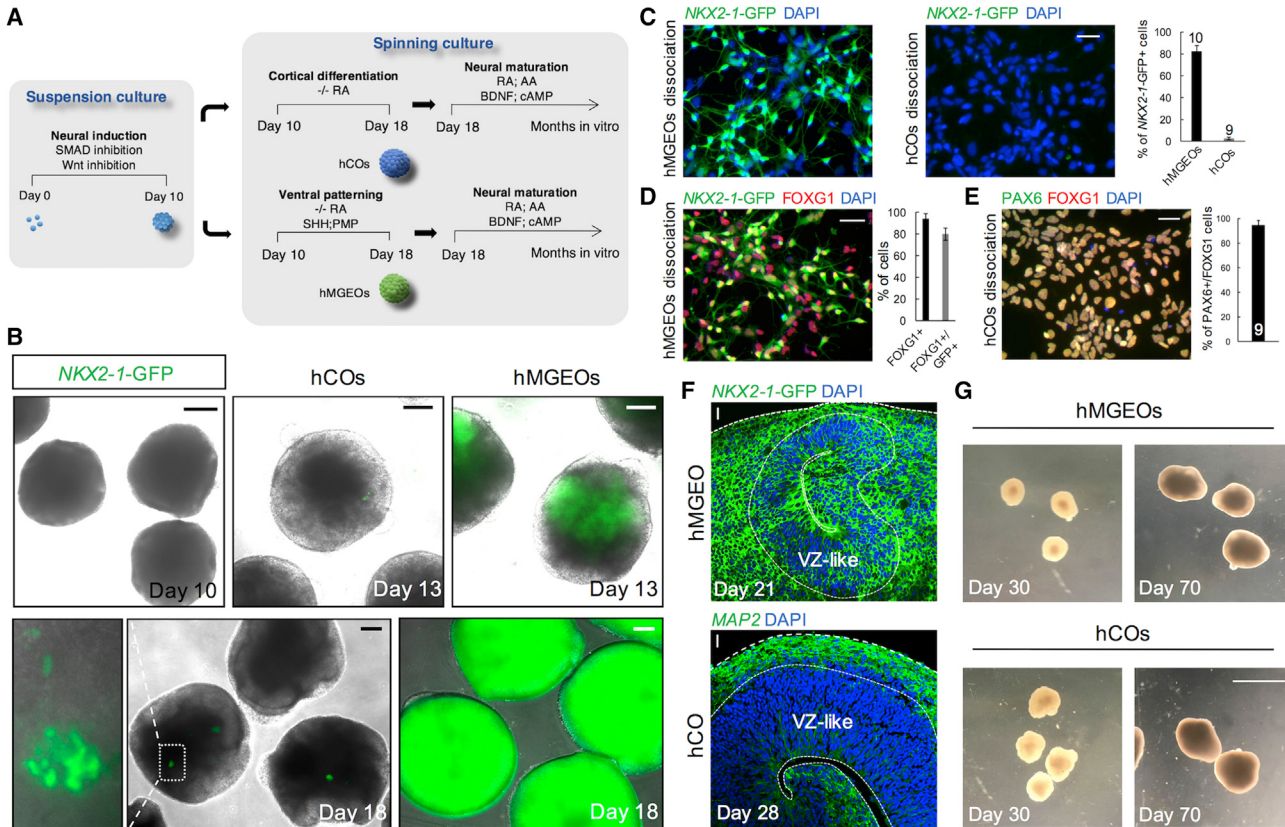


Figure 1. Generation of hMGEOS and hCOs

(A) Schematic view of the methods for generating hMGEOS and hCOs from hPSCs.

(B) Induction of *NKX2-1-GFP* in hMGEOS and hCO culture systems at different developmental stages. The scale bar represents 125 μm.

(C–E) Immunostaining and quantification of GFP (C), GFP and FOXG1 (D), and PAX6 and FOXG1 (E) in dissociated culture of hMGEOS and hCOs (day 21). Mean ± SD for hMGEOS (n = 10) and hCOs (n = 9) is shown. The scale bar represents 25 μm.

(F) Typical interior cellular organization of hMGEOS (3 weeks old) and hCOs (4 weeks old). The scale bar represents 20 μm.

(G) Morphology and size of hMGEOS and hCOs after 30 days and 70 days of culture. The scale bar represents 4 mm.

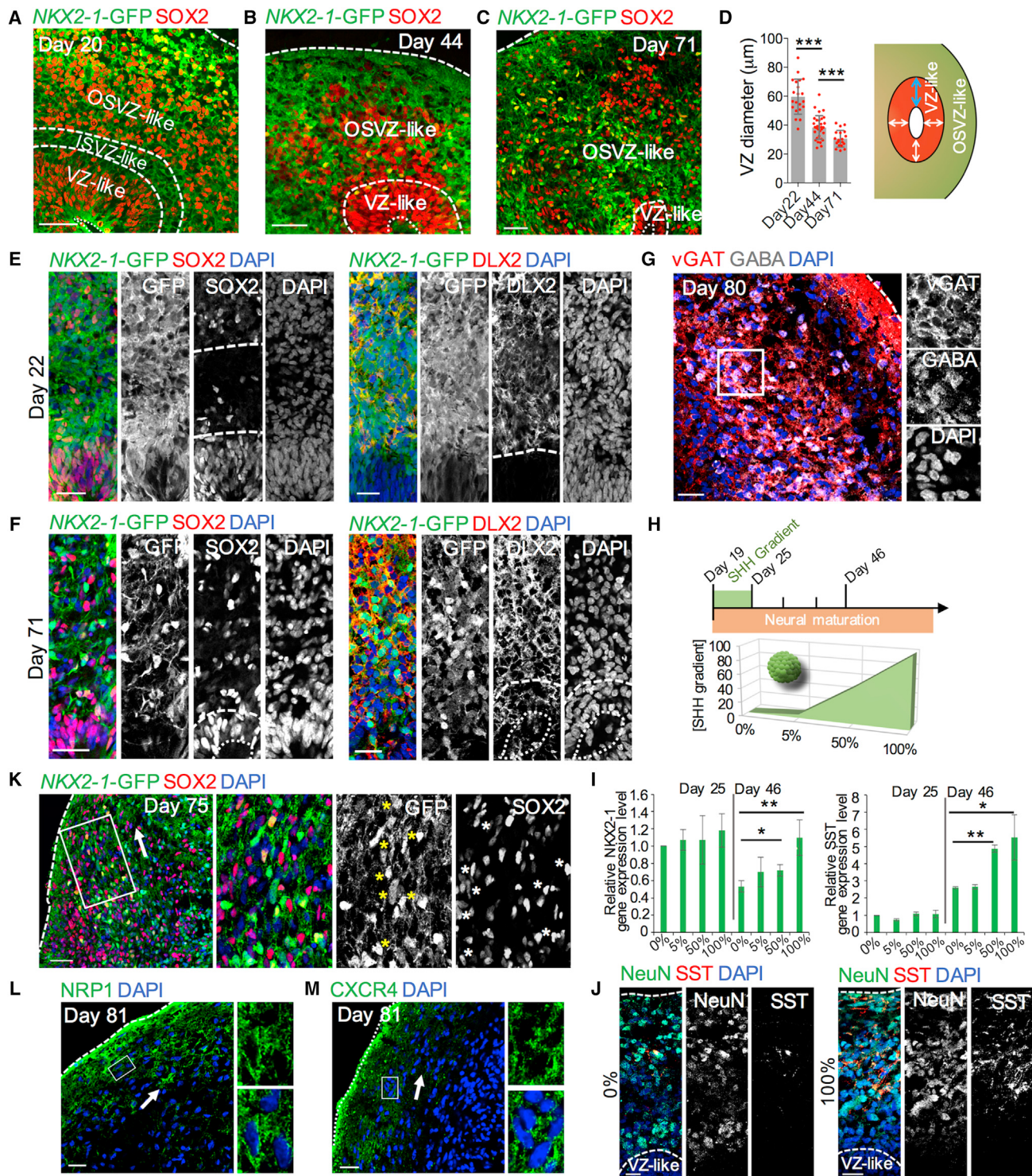
See also Figure S1.

committed during development of hMGEOS, cells in VZ-like area also undergo fate transition from neuroepithelial stem cells to more committed interneuron precursors.

We found that vGAT and GABA, markers of GABAergic neurons, were widely expressed in hMGEOS as they matured (Figure 2G), suggesting the production of interneurons. Previous studies with mouse models showed that the dorsal and ventral subdivision of MGE preferentially produces interneurons expressing SST (somatostatin) and PV (parvalbumin), respectively (Tyson et al., 2015). To test whether human MGE development may have a similar dorsal-ventral fate determination in interneuron subtype production, we compared the effect of different doses of SHH on development of SST- and PV-expressing neurons (Figure 2H). High SHH dosage did not significantly enhance *NKX2-1* expression at early stage but rather maintained *NKX2-1* expression at higher level during further development (Figure 2I). However, SST expression significantly increased under higher SHH dosage as hMGEOS matured together with the dramatic increase of SST⁺ neurons (Figures 2I and 2J). We found the expression of neuropeptide Y (NPY), marking an interneuron subtype closely related to SST⁺ interneuron development (Won-

ders and Anderson, 2006), also significantly increased under stronger SHH activation (Figure S1E). However, we did not observe obvious changes in PV or calbindin (CALB) expression (Figure S1E). These results suggest a shift of hMGEO identity from ventral to dorsal subdivision with prolonged SHH exposure, although a complete dorsal shift might not be achieved under the tested conditions.

In the OSVZ-like area of hMGEOS, we observed a migratory stream of progenitor cells, either toward or parallel to the surface of hMGEOS (Figures S1F and S1G). The stream contained SOX2⁺/*NKX2-1-GFP*⁻ cells, SOX2⁺/*NKX2-1-GFP*⁺ cells, and SOX2⁻/*NKX2-1-GFP*⁺ cells, which coalesced into migratory streaks (Figure 2K). Neuropilin-1 (NRP1)⁺ and CXCR4⁺ cells were present in the migratory streaks, further confirming their migrating properties (Figures 2L and 2M). Similarly, migrating cell clusters were observed in MGE domain of human fetal brain tissues in previous studies (Hansen et al., 2013). Thus, cells in hMGEOS may adopt intrinsic migration programs during development, resembling their *in vivo* counterparts. We also found that a core region underwent cell death during long-term culture of hMGEOS (Figures S1H and S1I). However, a number of DLX2⁺

**Figure 2. hMGEos Recapitulate Human MGE Development**

(A–C) Immunostaining for SOX2 and GFP reveals the diminishment of VZ-like area in hMGEos at day 20 (A), day 44 (B), and day 71 (C). The scale bar represents 50 μm .

(D) Thickness quantification of VZ-like area in hMGEos after 22 ($n = 21$), 44 ($n = 32$), and 71 ($n = 19$) days of culture. The maximum diameter of each VZ-like area (indicated with arrows in the schematic diagram on the right) was used for quantification. Mean \pm SD is shown for each stage. *** $p < 0.001$.

(E and F) Immunostaining for GFP, SOX2, and DLX2 of day 22 (E) and day 71 (F) hMGEo sections. The scale bar represents 25 μm .

(G) Immunostaining for vGAT and GABA in 80-day-old organoid section. The scale bar represents 25 μm .

(H) Schematic illustrating the modification of hMGEo protocol to test effect of various SHH doses on dorsal-ventral patterning.

(legend continued on next page)

cells were still detected in the region (Figure S1I), indicating that differentiated interneurons existed before cell death.

hCOs Recapitulate Human Dorsal Cortical Organization

As observed in developing cortex of human brain, SOX2⁺ RGs inside hCOs were organized into radial structures, with the apical surfaces marked by the expression of neural specific N-cadherin (Figure 3A). Newborn neurons generated from RGs expressed neuron-specific class III beta-tubulin (Tuj1) and were located on the basal side of the VZ-like area (Figure 3B). Cells in VZ-like area also expressed PAX6, another marker for RGs of the pallium, whereas NeuN, indicative of differentiated neurons, was observed outside of the VZ-like area (Figure 3C). The radially arranged GFAP⁺ fibers in VZ area resembles RGs during corticogenesis in vivo (Figure 3D). We also examined the mitotic behavior of RGs by measuring the angle of the orientation relative to the apical surface of the hCOs. 75.35% ± 5.92% (n = 4 hCOs; mean ± SD) adopted a vertical orientation, whereas only a minority of the RGs adopted horizontal orientations (Figure 3E). Furthermore, the staining with phospho-histone H3 revealed that dividing RGs were mostly located near the apical surface of VZ-like area (Figure 3F). Cleavage pattern of mitotic RGs showed that the majority of RGs (57.50% ± 10.60%; n = 2 hCOs; mean ± SD; 42 cells were measured) cleave vertical to the apical surface (Figure 3G). Abundant oblique cleavage (35.45% ± 7.71%; mean ± SD) was also observed, but horizontal cleavage occurred infrequently (7.05% ± 2.90%; mean ± SD; Figure 3G). Thus, the mitotic behavior of RGs in hCOs resembles the trends previously observed in cerebral organoids and the ventricular zone of the fetal human brains (LaMonica et al., 2013; Lancaster et al., 2013).

The formation of an SVZ layer containing intermediate progenitor cells outside of the VZ is a distinctive feature of human neocortical development (Lancaster et al., 2013). We therefore examined hCOs for the presence of SOX2⁺ progenitors outside of VZ-like area (Figure 3H). Staining for the IPs marker TBR2 and the oRGs marker FAM107A confirmed the presence of SVZ-like area in hCOs (Figures 3I and 3J). Furthermore, horizontal reelin⁺ cells were present in the surface area of hCOs, indicating the production of Cajal-Retzius cells (Figure 3K). With further development of the hCOs, separation of early-born CTIP2⁺ and late-born SATB2⁺ neurons became prominent in CP-like area (Figure 3L), indicating the specification of deep and upper cortical layers.

Astrogenesis is another essential facet of corticogenesis. We examined the presence of astrocytes in the CP-like area of hCOs after longer culture (day 105) as reported before (Paşa et al., 2015). Importantly, we found that NeuN⁺ cells in the CP-like area were extensively intermingled with GFAP⁺ processes from astrocytes (Figure 3M). Similarly, neuronal processes stained by MAP2 were commingled with GFAP⁺ glia processes in the CP-like area (Figure 3N). These data indicate astrocytes were generated and intertwined with differentiated neurons as hCOs developed.

Differential Transcriptome and Chromatin Accessibility between hMGEOs and hCOs

To define the molecular profiles of organoids, RNA sequencing (RNA-seq) was performed in early (day 30) and late (day 72) stages of hMGEOs and hCOs as well as the parental hESCs. By comparing with published transcriptomes of 21 different human organs (Melé et al., 2015), we confirmed that hMGEOs and hCOs had the highest correlation with transcriptomes of human brain tissues (false discovery rate [FDR] < 0.001; Figure 4A). Gene Ontology (GO) analysis revealed that multiple sets of neural-development-related genes were significantly upregulated in hMGEOs and hCOs after day 30 with pluripotency genes downregulated (Figure 4B). Genes related with dendrite development, synapse organization, ion channel activity, and neurotransmitter secretion were similarly upregulated in hMGEOs and hCOs at both time points. On the other hand, more developed hCOs displayed significantly higher expression of genes for neurotrophic signaling and calcium ion transport (Rutherford et al., 1997; Simms and Zamponi, 2014). Importantly, hMGEOs and hCOs displayed differential regulation of genes related to cell fate commitment (Figure 4B).

Analysis of differentially expressed genes revealed that transcription factors specifying MGE (e.g., NKX2-1, NKX6-2, DLX1, OLIG1, and FOXA2) were uniquely expressed in hMGEOs (Figures 4B and 4C). GABA synthesis enzymes, GAD1 and GAD2, were highly expressed in hMGEOs and were also expressed in hCOs at late time point, indicating hCOs also produced GABAergic neurons without exogenous ventral patterning cues. Glutamatergic neuron markers GLUD1, vGLUT1, and vGLUT2 were highly enriched in hCOs. PAX6, NEUROG2, TBR1, and CTIP2, which regulate cortical neuron differentiation, were also enriched in hCOs. In addition, multiple genes involved in early neurogenesis (e.g., NES and NEUROG1) were commonly upregulated in hMGEOs and hCOs. Comparison with transcriptomes of multiple human fetal brain regions (Miller et al., 2014) revealed that hMGEOs and hCOs are most close to MGE and cortical domains (occipital neocortex [OCX] and orbital frontal cortex [OFC]), respectively (FDR < 0.001; Figure 4D). Overall, these results demonstrate hMGEOs and hCOs molecularly resemble the developing human MGE and cortex.

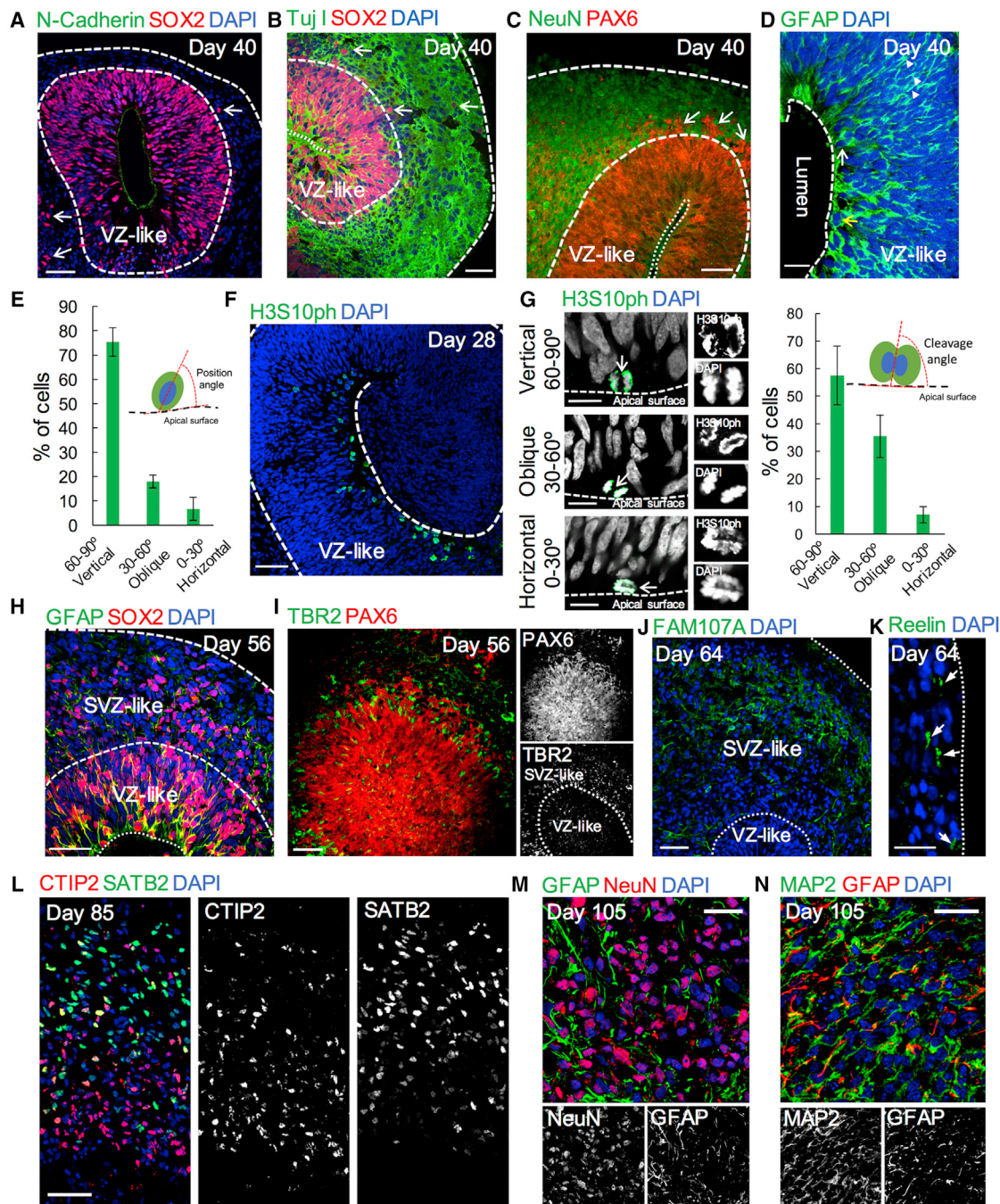
To understand transcriptional regulation in human MGE and cortex development, we focused on alterations in chromatin accessibility, a key epigenetic regulation of transcription in the brain. We profiled genome-wide chromatin accessibility of 72-day-old hMGEOs, hCOs, and their parental ESCs by assay for transposase-accessible chromatin with high-throughput sequencing (ATAC-seq). Differentially open chromatin regions (dOCRs) were identified between organoids and ESCs. Over 10,000 increased and over 20,000 decreased dOCRs were found after differentiation from ESCs to either hMGEOs or hCOs (Figure S2). Open chromatin was observed preferentially for genes activated during organoid development ($p < 2.2 \times 10^{-16}$), with closed chromatin in suppressed genes

(I) qRT-PCR analysis of NKX2-1 and SST expression. Mean ± SD is shown for each condition (n = 4). **p < 0.01; *p < 0.05.

(J) Immunostaining for SST in 46-day-old hMGE sections. The scale bar represents 25 µm.

(K–M) Representative images showing migrating streaks interior of 75-day-old hMGEOs. The migration directions are indicated with arrows. Immunostaining was performed for GFP and SOX2 (K), NRP1 (L), and CXCR4 (M). The scale bar represents 50 µm in (K) and 25 µm in (L) and (M).

See also Figure S1.

**Figure 3. hCOs Recapitulate Human Dorsal Cortical Organization**

(A) Immunostaining for SOX2 and N-cadherin in hCO section (40 days old). Arrows show potential oRGs outside of VZ-like area. The scale bar represents 50 μ m.

(B and C) Immunostaining for SOX2 and Tuj1 (B) and PAX6 and NeuN (C) in hCO sections (40 days old). Arrows show potential oRGs outside of VZ-like areas. The scale bar represents 50 μ m.

(D) GFAP staining in hCO section (40 days old). Arrowhead, glial fibers; white arrow, vertically located RG cell; yellow arrow, horizontally located RG cell. The scale bar represents 20 μ m.

(E) Quantification of position angle of RGs located at the lumen surface. Mean \pm SD is plotted ($n = 4$ VZ-like area from four of 40-day-old hCOs).

(F) Immunostaining for phospho-histone H3 in hCOs section (4 weeks old). The scale bar represents 50 μ m.

(G) Representative images of vertical, oblique, and horizontal cleavage of dividing RGs in VZ-like area of 4-week-old hCO section (left). Mean \pm SD is plotted for each category ($n = 42$ cells). The scale bar represents 10 μ m.

(legend continued on next page)

($p < 3.32e-5$; left and right panel in Figure 4E). Genes involved in dendrite development commonly displayed open chromatin conformation in both hMGEOS and hCOs (Figure 4F). Meanwhile, hMGEOS and hCOs showed subsets of dOCRs enriched for genes specifically expressed in hMGEOS ($p = 2.02e-3$) or hCOs ($p = 4.44e-4$; bottom panel in Figure 4E). Notably, chromatin regions related to oligodendrocyte genes were specifically open in hMGEOS, and those involved in endothelium development were specifically open in hCOs. Importantly, open chromatin regions unique to hMGEOS were observed in genes critical in MGE development (e.g., NKX6-2, FOXA2, OLIG2, and DLX6), whereas genes involved in cortex development (e.g., PAX6, MGP, GLI3, and EMX2) displayed hCOs-specific open chromatin regions (Figure 4G). Therefore, our results suggest an active role of chromatin accessibility in transcriptional regulation during MGE and cortex development.

Lineage Specification during hMGEOS and hCO Development

To better understand cell type specification during organoid development, we performed single-cell RNA-seq (scRNA-seq) in organoids (Figure 5A). After quality control, data from a large number of single cells (59,235 cells in total) from two biological replicates of hMGEOS and hCOs at two developmental stages (early: day 30; late: day 72~79) were obtained (Figures 5A and S3A). Analysis by t-distributed stochastic neighbor embedding (t-SNE) revealed production of both unique and overlapping cell types between hMGEOS and hCOs (Figure 5B). Compared with those at day 30, hMGEOS and hCO cells at day 72~79 were more distinct, indicating progression of further lineage commitment during the organoid development. Batch effect between two replicates was minimized by regressing out cell-cell variation in gene expression driven by batch ($p > 0.308$; Figure S3B; Macosko et al., 2015). Almost exclusive expression of TBR1, a marker unique for cortical excitatory neurons (referred to as cortical neuron [CN]), or GFAP for astrocytes confirmed a minimal doublet rate in our scRNA-seq (Figure S3C).

To characterize each cell, cells from organoids were clustered into 29 clusters according to their transcriptome features (Figures S3D–S3G). Notably, no significant difference in mapping ratio and total number of unique molecular identifiers (UMIs) were found among different clusters (Figure S4A). GO analysis and expression pattern of unique markers functionally annotated each cluster (Figure 5C). First, we isolated ten “neuronal” clusters by the high expression of general neuronal markers (STMN2, GAP43, and DCX) and the lack of early neurogenesis genes (VIM, NES, and HES1; Figures S3F and S3G). Interneurons, marked by GAD1 and the interneuron-specific neuropeptides TAC1, were significantly enriched in five neuronal clusters (IN1–5) from hMGEOS, whereas hCOs also generated interneurons (Figures 5D and 5E). hMGEOS rarely produced cortex-specific cell types (CN1–2). TBR1⁺ and NEUROD2⁺ cortical neurons were mainly from hCOs (Figure 5D). Comparative analysis of hMGEOS- and hCOs-derived interneurons revealed that

NKX2-1 expression was negligible in hCOs-derived interneurons (Figure 5F). Some neurodevelopmental genes (e.g., MAP2 and ALCAM) were enriched in hMGEOS-derived interneurons, whereas hCOs-derived interneurons displayed higher cortical developmental genes (e.g., ZIC1, PTN, and MEIS2; Inoue et al., 2007; Manuel et al., 2015; Figure 5G), indicating the differential identities among hMGEOS- and hCOs-derived interneurons. Three neuronal clusters show no enrichment of markers for interneuron or cortical neuron and thus were annotated as non-committed neurons (neuron1–3). These clusters were from both hMGEOS and hCOs and decreased with further organoid development (Figure 5H).

Comparison with the published single-cell transcriptome from human brain tissues (Darmanis et al., 2015) further confirmed that ten neuronal clusters resemble the differentiated neurons (Figure S4B). In addition, three non-neuronal clusters, which are mainly derived from early stage of organoids, were significantly correlated with neural progenitor cells (NPC1–3). Cell-cycle- and chromatin-related genes were enriched, and pluripotent genes were completely downregulated in NPCs (Figures S4A and S4C). Interestingly, we noticed that the IP marker TBR2 may also express in differentiated neurons, as revealed by its co-expression with TBR1 (Figure S4D). Four non-neuronal clusters were exclusively derived from hCOs. Subplate cell identity (PCP4⁺ and PLS3⁺) was present in three of them (SP1–3; Figures 5D and 5H), and the other cluster displayed significant enrichment of cilium development and was annotated as ependymocytes (EPs). The other six non-neuronal clusters show no functional characters. These clusters displayed weak enrichment for NPC character but lacked mature neuronal identity (Figure S4B) and thus were classified as intermediate progenitors. Three of the six intermediate clusters highly expressed ATP and oxidoreduction metabolic genes and were marked as high-metabolic intermediates (HMI1–3). Because the metabolic process is known to switch from aerobic glycolysis to oxidative phosphorylation throughout neuronal development (Zheng et al., 2016), HMIs are perhaps progenitor cells undergoing adaptation of energy metabolism.

We found that genes related to oligodendrocyte development were present in five non-neuronal clusters (Figure S3G). Transcription factors controlling oligodendrocyte maturation (OLIG1 and OLIG2) were present in only one of these clusters (OL). Two clusters displayed higher expression of astrocyte-related genes than oligodendrocyte-related genes (AS1–2). Interestingly, astrocytes (marked by S100B and GFAP) were derived from both hMGEOS and hCOs, suggesting that human MGE cells give rise to progenitors for astrocytes, which is consistent with the recent observation of astrocyte production in NKX2-1 expressing mouse ventral telencephalon (Minocha et al., 2015). One cluster that lacked both oligodendrocyte and astrocyte-related genes but expressed gliogenesis genes was annotated as glia progenitor cell (GPC).

Importantly, we found oligodendrocyte progenitors (OPC1–2; marked by S100A10 and CD44) arose mostly from hMGEOS,

(H–J) Immunostaining for SOX2 and GFAP (H), PAX6 and TBR2 (I), and FAM107A (J) in hCO section (56–64 days old). The scale bar represents 50 μ m.

(K) Immunostaining for reelin in hCO section (64 days old). The scale bar represents 25 μ m.

(L) Separation of deep-layer CTIP2⁺ neurons and upper-layer SATB2⁺ neurons in hCO section. The scale bar represents 50 μ m.

(M and N) Immunostaining for GFAP and NeuN (M) and GFAP and MAP2 (N) in hCO sections (105 days old). The scale bar represents 25 μ m.

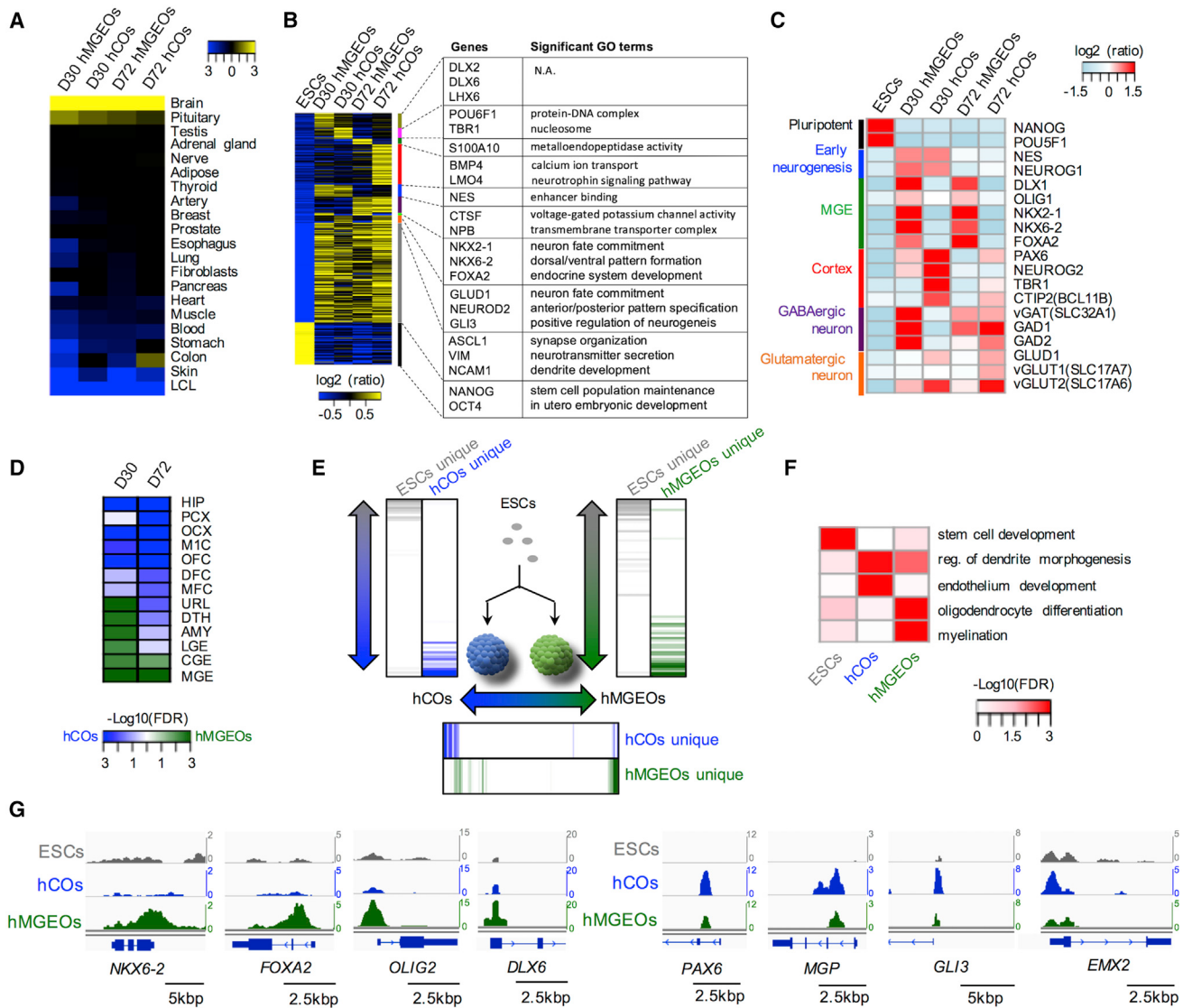


Figure 4. Transcriptome and Chromatin Accessibility during hMGEO and hCO Development

- (A) Enrichment of tissue-specific genes. Enrichment and depletion are scaled by $-\log_{10}(\text{FDR})$ and shown in yellow and blue colors, respectively.
 - (B) Differentially expressed genes during organoid development. Representative genes and GO terms ($\text{FDR} < 0.05$) are shown in right panel.
 - (C) Expression profile of key genes related to MGE and cortical development.
 - (D) Gene set enrichment analysis (GSEA) of gene signatures for in vivo embryonic brain region. Enrichment of gene signatures ($-\log_{10}(\text{FDR})$) in hCO and hMGEO is shown in blue and green, respectively.
 - (E) Relationship between gene expression change and chromatin architecture during organoid development. Genes are sorted by $\log_2(\text{ratio})$, and the presence of dOCRs is shown by colors.
 - (F) GO enrichment of target genes of dOCRs. $-\log_{10}(\text{FDR})$ is colored in red.
 - (G) ATAC-seq read distribution around the transcription start site (TSS) of in vivo MGE and cortex-specific gene signatures.
- See also Figure S2.

and until late stage, only a limited number of OPCs were produced from hCOs (Figure 5H). Meanwhile, mature oligodendrocytes (OL) were exclusively produced from hMGEOs. To confirm this differential pattern of oligodendrocyte formation in hMGEOs and hCOs, we mapped the single-cell transcriptome of primary AS, OPC, and OL from published human brain tissues (Darmanis et al., 2015) and found AS, OPC, and OL produced from hMGEOs displayed significant correlation with their in vivo counterparts (Figure S4E). Furthermore, im-

munostaining for OLIG1 in late stage (day 81) organoids confirmed that OLIG1⁺ cells were uniquely produced in hMGEOs (Figure 5I). Similarly, previous neurodevelopmental studies in mouse identified the first OPC wave in MGE and entopeduncular area of ventral forebrain (Kessaris et al., 2006). Thus, our results suggest that, during human brain development, MGE and cortex also display distinct timelines for oligodendrocyte genesis, with oligodendrocyte genesis from MGE preceding the cortex.

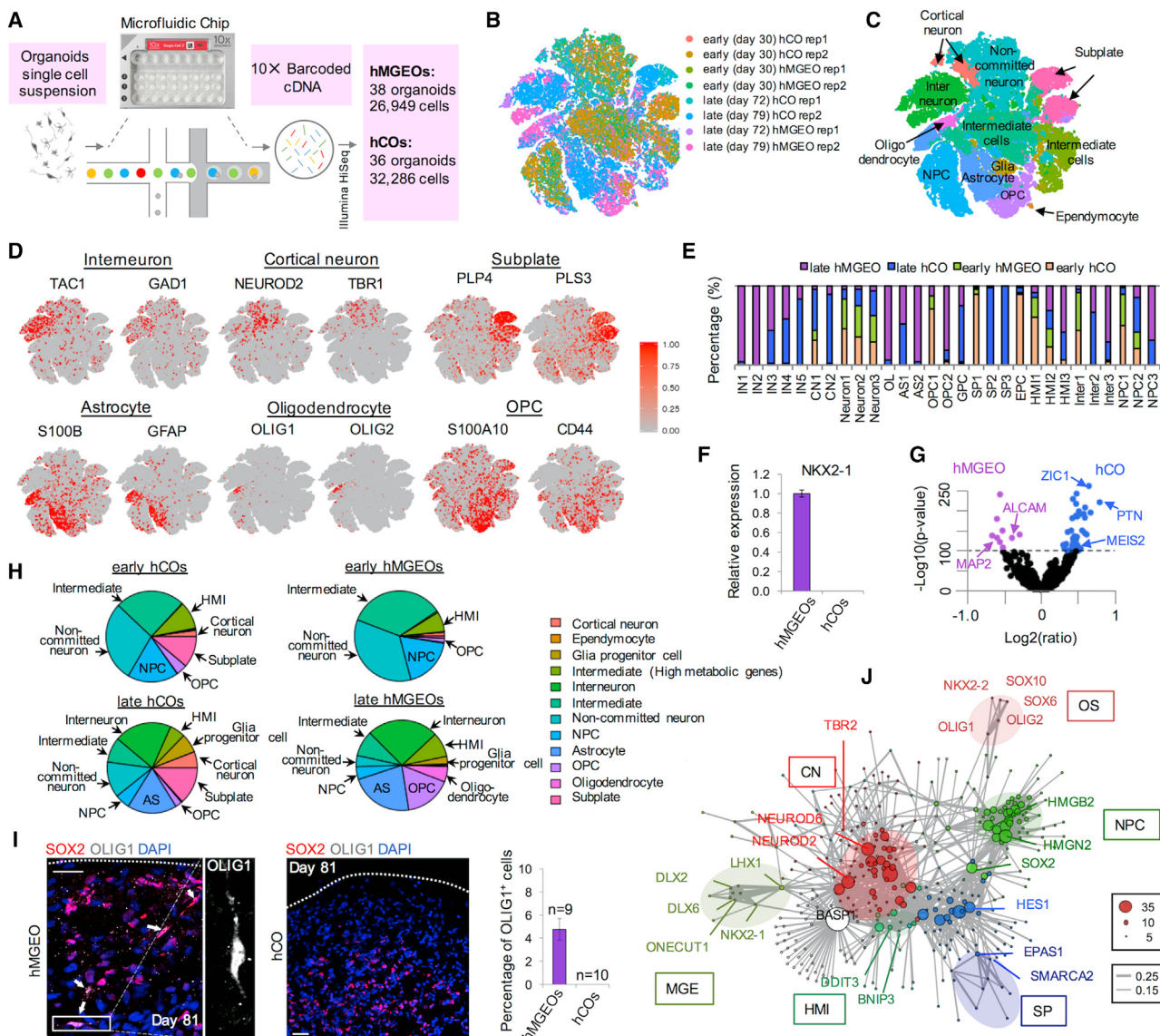


Figure 5. scBNA-Seq Analysis of hMGEOs and hCOs

(A) Strategy for scRNA-seq with Chromium system.

(B) tSNE plot of single cells distinguished by (B) organoids and (C) annotation of clusters.

(D) Expression patterns of markers for different cell types produced in hMGEQs and hCOs

(D) Expression patterns of markers for different cell types produced
 (E) Percentage of cells from hMGEQs and hCOs in all clusters

(F) Differential expression of NKX2-1 between hMGEo- and hCO-derived interneurons. Average read count is normalized to that of hMGEo-derived interneurons. Mean ± SEM are plotted.

(G) Comparison of transcriptome between hMGEO- and hCO-derived interneurons. Genes with $-\log_{10}(p \text{ value}) \geq 100$ are shown in violet (hMGEO) and blue (hCO).

(4) Ratios of all the other histone modifications

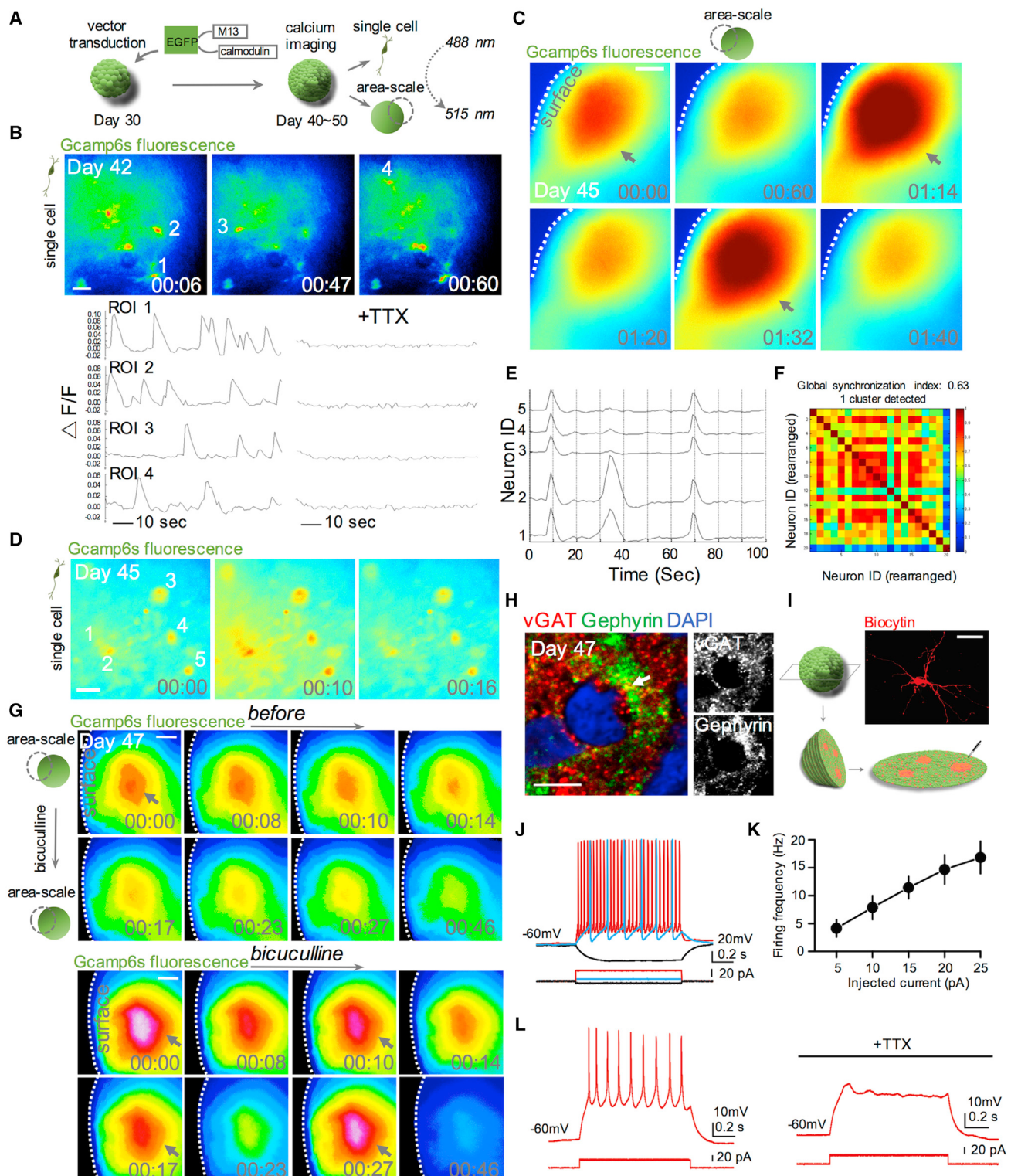
(I) Immunostaining and quantification for OLIG1 in 81-day-old sections of hMGEs and hCOs. Mean \pm SD is plotted for each condition. Sections from eight hMGEs and six hCOs were used for quantification.

(J) Co-expression network of transcriptional and epigenetic regulators. Edge size represents Pearson correlation coefficient. Node size represents the number of interactions. The size of each node is proportional to the number of interactions.

connections. Examples of ec

Because hMGEos and hCOs exhibited striking parallels to the developing human MGE and cortex, we next sought to identify key regulators involved in lineage specification. We constructed a co-expression network of transcriptional and epigenetic

netic regulators. The network showed two dense and several smaller subnetworks (Figure 5J). The densest subnetwork (green) included transcription factors expressed in NPCs (e.g., HMGB2) and represented the network of basal transcriptional

**Figure 6. Efficient Functional Maturation of hMGEOS**

(A) Schematic view of the methods for calcium imaging of intact hMGEOS.

(B) Representative image showing cells expressing hsyn-GCaMP6s in intact 42-day-old hMGEOS. The single cell tracings of calcium transient (region of interest [ROI] indicated on top) are shown, which are blocked by application of TTX (1 μ M). The scale bar represents 25 μ m.(C) Representative image of area-scale calcium imaging in intact 45-day-old hMGEOS. The synchronized calcium surges are indicated with arrows. Time is shown in min:s. The scale bar represents 100 μ m.

(legend continued on next page)

factors (Figure S4F). Cortical neuronal markers (NEUROD6 and CTIP2) were detected in the second densest subnetwork (red), whereas interneuron markers (NKX2-1 and DLX6) were in a small subnetwork (olive green). Cut homeobox family transcription factor, ONECUT1, whose function in MGE development has not been fully explored, was directly connected to NKX2-1 and DLX6 in the network and uniquely expressed in interneurons (Figure S4F). Another interneuron marker, LHX1, was a hub factor connecting the interneuron subnetwork with others. We also found that functionally unknown transcription factors were enriched in high metabolic intermediate progenitors (BNIP3 and DDT3) and in subplate cells (EPAS1 and NR4A1). Overall, our results demonstrate that hMGEOS and hCOs recapitulate lineage productions in the developing human MGE and cortical domains and provide a resource to dissect cell identities and key regulators for human brain development.

Efficient Functional Maturation of hMGEOS and hCOs

To examine whether our organoid culture system produced functionally active neurons, we utilized the genetically encoded calcium indicator GCaMP6s under human synapsin I promoter (Figure 6A). Neurons inside hMGEOS differentiated for 40~50 days already displayed calcium transients, which were blocked by adding Na^+ channel blocker tetrodotoxin (TTX) (Figure 6B; Movie S1), indicating these calcium oscillations were neuronal activity dependent. Importantly, when we performed calcium imaging over larger fields of view, we found that hMGEOS showed areas with highly synchronized calcium surges (Figure 6C; n = 3 hMGEOS; with one to two synchronized areas observed for each hMGEOS), representing the functional neuronal networks. The synchronized pattern of neuronal activity within the organoids was further investigated by performing higher magnification imaging where individual neurons displayed calcium surges simultaneously (Figures 6D and 6E). Synchronization matrix analysis based on calcium spike patterns of individual neurons further revealed the presence of synchronized neuron clusters inside the hMGEOS (Figure 6F). Treating hMGEOS with bicuculline, an antagonist of GABA_A receptors, robustly enhanced synchronization of calcium surges in the areas of the organoids, suggesting that GABAergic inhibition controls neuronal synchronization (Figure 6G; n = 2 hMGEOS). Furthermore, histological analysis of hMGEOS revealed the presence of an extensive network of vesicular GABA transporter (vGAT) puncta, marking pre-synaptic structures of GABAergic synapses. Gephyrin, the post-synaptic scaffold protein essential for inhibitory synapses, showed similar subcellular distributions adjacent to vGAT puncta (Figure 6H), confirming inhibitory synaptogenesis in hMGEOS.

We also examined the electrophysiological properties of cells in hMGEOS by whole-cell patch-clamp recording (Figure 6I; see STAR Methods for details) that revealed that 8 of 14 recorded cells exhibited APs (Figure 6J). Increasing injection current resulted in an increase in firing frequency of the recorded neurons (Figure 6K; from 4.2 ± 1.5 Hz, +5 pA to 16.8 ± 2.9 Hz, +25 pA; n = 7 cells). TTX completely abolished APs in all tested cells (Figure 6L; n = 3). The neuronal morphologies of recorded cells were confirmed by injecting biocytin into the cells during the patch-clamp recordings (Figure 6I).

We then tested the functional maturation of hCOs. As early as day 45, hCOs started to show active calcium transient, which was already synchronized and could be blocked by TTX (Figure S5C). We found neuronal disinhibition by bicuculline largely induced synchronization of calcium surges at area scale, with the effect even stronger than observed in hMGEOS (Figure S5D; Movies S2 and S3; n = 2 hCOs). Furthermore, staining for pre-synaptic protein synapsin-1 (SYN1) and post-synaptic protein PSD95 confirmed abundant synaptogenesis within hCOs at this stage (Figure S5E). Together, these results demonstrate that functional neurons were generated and neuronal networks were efficiently established in hMGEOS and hCOs.

Fusion of hMGEOS and hCOs Recapitulates Cortical Migration of Human Interneurons

The generation of hMGEOS and hCOs led us to establish an organoid-based platform to study human interneuron migration. We noticed extensive neuronal migration in hMGEOS embedded inside Matrigel droplets, typically with individual neurons migrating to the surface of the embedding matrix (Figures S6A–S6D). Similarly, hCOs displayed active neuronal migration inside Matrigel (Figure S6E). We then confirmed a robust interneuron migration across organoids by fusing hMGEOS derived from H1 hESCs and *NKX2-1*^{GFP/W} HES3 cells (Figure S6F). These results revealed the remarkable potential of brain organoids for studying the migration of inhibitory neurons.

To mimic tangential migration of interneuron progenitors, we fused hMGEOS and hCOs together to generate the fused MGE-cortical organoids (hfMCOs) (Figure 7A). To monitor migration, hMGEOS were infected with lentivirus expressing red fluorescent protein (RFP) under human synapsin I promoter. RFP-labeled neurons gradually migrated from MGE side toward hCOs, and large number of RFP-labeled hMGEOS cells were found at hCO side (Figure 7B). Because no *NKX2-1*-GFP⁺ cells were detected in hCOs after long-term culture (Figures 4C and 5F), we performed further characterization of *NKX2-1*-GFP⁺ interneuron migration without RFP labeling. 3D reconstitution

(D and E) Calcium imaging of synchronized area (C) at single cell level. ROIs are indicated (D), and tracings of single-cell calcium surges are shown (E). Time is shown as min:s. The scale bar represents 25 μm .

(F) Synchronization matrix of calcium surges from recorded single neurons in intact 45-day-old hMGEOS.

(G) Area-scale calcium imaging reveals bicuculline disinhibition enhanced area synchronization of calcium surges in intact hMGEOS (47 days old). Arrows in bicuculline-treated group indicate the synchronized calcium surge, whereas there is no synchronization in the same area before bicuculline treatment. Time is shown as min:s. The scale bar represents 100 μm .

(H) Immunostaining for pre-synaptic protein vGAT and post-synaptic protein gephyrin in 47-day-old hMGEOS section. The scale bar represents 5 μm .

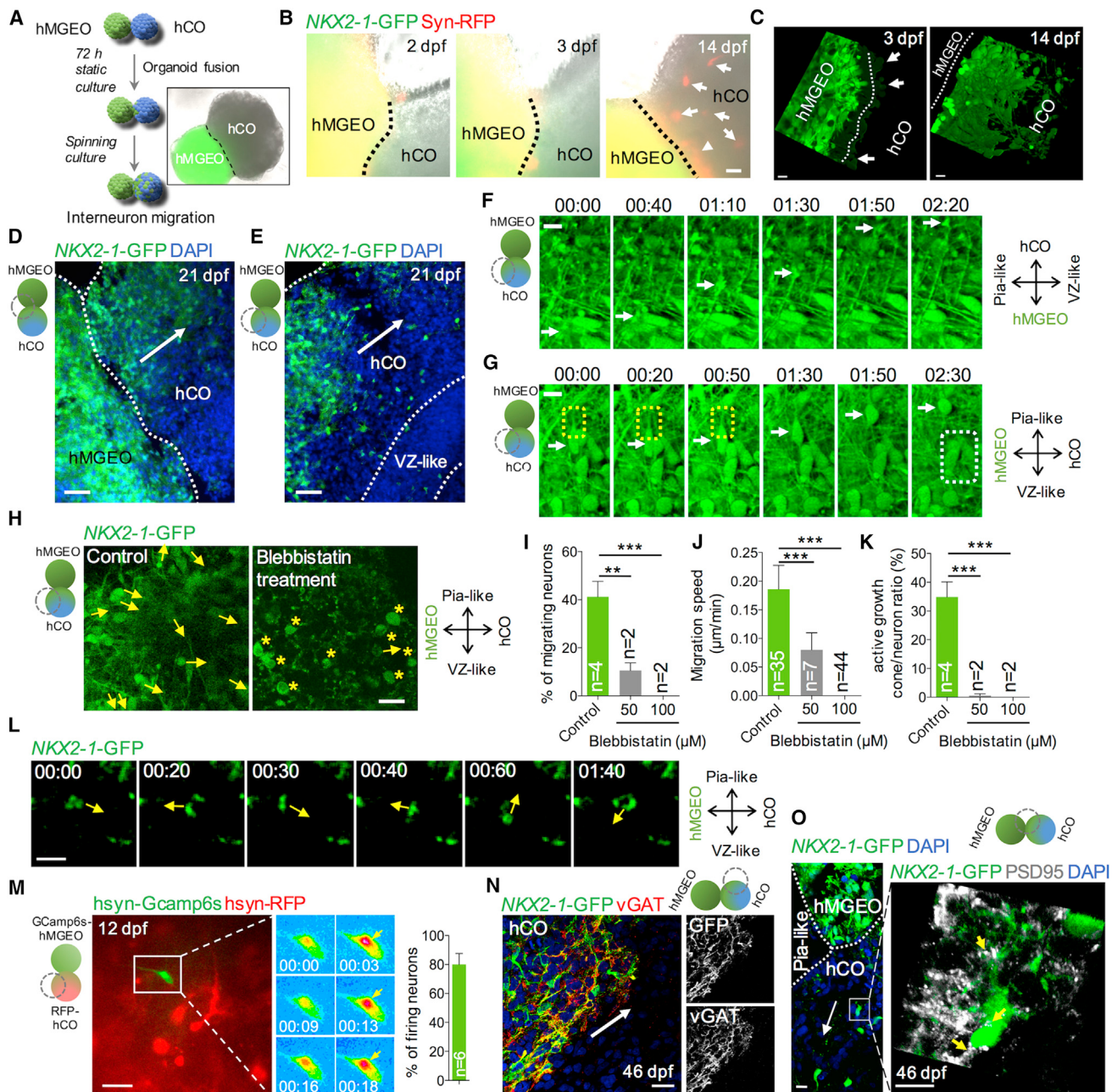
(I) Diagram showing slice patch clamp and identification of the neuronal morphology of the recorded cell by filling with biocytin. The scale bar represents 25 μm .

(J) Representative voltage traces of current-clamp recordings of a cell in hMGEOS slice in response to current steps (-5 pA, $+5$ pA, and $+25$ pA from -60 mV, 1 s).

(K) Graph depicting the firing frequency of the recorded cells from hMGEOS plotted against injected current (n = 7 cells). Mean \pm SE is shown.

(L) Representative image of APs of a cell in hMGEOS slice before and during application of TTX (1 μM).

See also Figure S5 and Movies S1, S2, and S3.

**Figure 7. Modeling Human Interneuron Migration using hfMCOs**

(A) Scheme illustrating the strategy of organoids fusion for modeling human interneuron migration.

(B) Images showing hsyn-RFP-labeled MGE progenitors (arrows) migrated toward hCO side during culture. dpf, days post-fusion. The scale bar represents 10 μm.

(C) 3D reconstruction of hfMCOs revealed the migration of *NKX2-1*-GFP⁺ progenitors in hCO side. Z stack confocal imaging was performed near the fusion border. Note that cells have already started to migrate out 3 dpf (arrows). The scale bar represents 10 μm.

(D and E) Immunostaining for GFP in hfMCOs section near (D) or away from (E) the fusion border 21 dpf confirmed the migration of MGE progenitors. Arrows show migration directions. The scale bar represents 40 μm.

(F and G) Representative images showing typical forward movement of growth cone (F, arrows) and soma translocation observed for migrating *NKX2-1*-GFP⁺ progenitors (G, arrows) at 14 dpf. White box, neurons that migrated out of the focal plane; yellow box, cytoplasm elongation proceeding nucleokinesis. The scale bar represents 10 μm.

(H) Representative images showing migration directions of *NKX2-1*-GFP⁺ progenitors in hfMCOs without (left) or with 50 μM blebbistatin treatment (right). Yellow arrows, migration directions; yellow stars, neurons without migration detected. The scale bar represents 10 μm.

(I–K) Quantification of ratio of migrating neurons (I), migrating speed (J), and ratio of active growth cones (K). Mean ± SD is plotted. **p < 0.01; ***p < 0.001.

(legend continued on next page)

of the fusion border between hMGEo and hCO revealed that, at 3 days post-fusion (dpf), *NKX2-1-GFP*⁺ progenitors already started to egress and extensive progenitor migration was observed 2 weeks later (Figure 7C). Furthermore, immunostaining of hfMCOs cryosections confirmed that the *NKX2-1-GFP*⁺ progenitors migrated between organoids (Figure 7D). In total, all 42 hfMCOs that we generated showed migration of *NKX2-1-GFP*⁺ cells from hMGEo to hCO. We found that the majority of the migrating cells were confined to the superficial areas of hCOs. Histological analyses confirmed that migration routes of *NKX2-1-GFP*⁺ progenitors were outside of cortical VZ-like area (Figures 7E and S7A), which is consistent with the reported pattern of interneuron tangential migration (Ma et al., 2013). Indeed, we found that the migration required the proper development of SVZ/CP-like area in hCOs, without which migration was inefficient. In this condition, migration routes might be altered toward the inner side of hCOs but were excluded from VZ-like area (Figures S7B and S7C).

To further characterize the migration behavior, we performed 4D (x, y, z, and t) imaging of live hfMCOs near the fusion border at 2 weeks after fusion (Movie S4). We found two key features of migrating *NKX2-1-GFP*⁺ cells in hfMCOs: (1) directed forward extension of leading process (Figure 7F) and (2) nucleokinesis following the leading process (Figure 7G). Importantly, cytoplasm elongation was often observed preceding nucleokinesis (Figure 7G). These behaviors are remarkably similar to previous reports of interneuron migration in live mouse embryos, mouse MGE explant models, and postmortem human brain sections (Bellion et al., 2005; Ma et al., 2013; Paredes et al., 2016; Yanagida et al., 2012), demonstrating the suitability of using hfMCOs to study human interneuron migration.

Nonmuscle myosin II may be one of key regulators of directed cell migration, including the migrating mouse MGE cells (Bellion et al., 2005). We found treatment with blebbistatin, a known myosin II inhibitor, completely blocked cell migration, with *NKX2-1-GFP*⁺ cells scarcely identified in hCO side under continuous drug treatment (Figure S7D). To monitor the effect of inhibiting myosin II in real time, we allowed cells to migrate uninterrupted for 2 weeks and then performed live-cell imaging on the hCO side with blebbistatin treatment. We found that soma translocation of interneuron progenitors was dramatically decreased with 50 μM blebbistatin treatment (10.55% ± 2.25%; n = 2 hfMCOs; 63 cells in total; mean ± SD) compared with control hfMCOs (41.23% ± 3.20%; n = 4 hfMCOs; 79 cells in total; mean ± SD) within 10 hr, and 100 μM blebbistatin treatment completely abolished migration (n = 2 hfMCOs; 44 cells in total; mean ± SD; Figures 7H and 7I; Movies S5 and S6). The average migrating speed of interneuron progenitors was 0.19 ± 0.01 μm/min (n = 35 cells from four hfMCOs; mean ± SD; Figure 7J), which was close to the speed observed from living embryo but slower than that obtained from MGE explant

culture (Bellion et al., 2005; Yanagida et al., 2012), indicating that the cellular environment of hfMCOs might closely approximate their in vivo counterparts. With myosin II inhibition, the migration speed largely decreased (Figure 7J). Importantly, we found a near-complete blockage in directed movement of leading process, even under lower dosage of blebbistatin (Figure 7K). Instead of forward outgrowth, growth cones under blebbistatin treatment only displayed local swing-like movement without any directional preference (Figure 7L), indicating a critical role of myosin II in growth cone dynamics of migrating interneurons. These results demonstrate that nonmuscle myosin II plays a critical role in soma translocation and growth cone dynamics of migrating human MGE progenitors.

To examine the neuronal activity of migrating interneurons, we generated hfMCOs by fusing hsyn-GCaMP6s-labeled hMGEo with hsyn-RFP-labeled hCO and measured the calcium transient at the hCO side of hfMCOs. A robust calcium transient at hCO side was observed with 80.40% ± 7.80% of detected cells (n = 6 hfMCOs; mean ± SD; 85 cells in total) and with active calcium surges as early as 12 dpf (Figure 7M), indicating that migrating interneurons developed a normal neuronal activity. Furthermore, neurons from hMGEo maintained the GABAergic identity during migration, as revealed by the expression of GABAergic marker vGAT (Figures 7N and S7E). Importantly, migrated interneurons displayed a normal neuronal morphology and formed excitatory post-synaptic densities both at the soma and neurite areas (Figure 7O), further confirming their integration into local neuronal network of hCOs. Together, our data demonstrate that hfMCOs serve as a model for human interneuron migration with a 3D cellular environment.

DISCUSSION

Multiple lines of investigation have examined neuronal development in brain-specific organoids to date, mostly focusing on cortical development. Midbrain- and hypothalamus-specific organoids were also generated (Jo et al., 2016; Qian et al., 2016), but methods to derive organoids resembling other brain areas are less developed, with the exception of two very recent studies reporting on ventrally specified organoids, which we discuss further below (Bagley et al., 2017; Birey et al., 2017). Here, we describe strategies to generate human brain organoids mimicking the MGE or cortex domain. Notably, we describe a robust method for generating human MGE organoids to study human interneurogenesis and migration in 3D cultures.

In forming organoids, we and others (Mariani et al., 2012; Paşa et al., 2015) do not include Matrigel as supportive matrix, but there are reports suggesting the protective effects of Matrigel in organoid culture (Kadoshima et al., 2013; Qian et al., 2016). We found that Matrigel embedding does not improve the formation of hMGEos and hCOs in our system. However,

(L) Representative images of random movement of growth cone in the presence of 50 μM blebbistatin. Yellow arrows, movement directions. The scale bar represents 5 μm.

(M) Representative image showing hsyn-GCaMP6s-expressing interneuron migrated into RFP-labeled hCO in an intact hfMCO at 12 dpf (left), the spontaneous calcium surges (middle), and the quantification (right). Mean ± SD is plotted (n = 6; totally 85 cells). The scale bar represents 20 μm.

(N) Immunostaining for vGAT and GFP in section of hfMCO. Arrow indicates the migration direction. The scale bar represents 20 μm.

(O) Immunostaining for PSD95 and GFP in section of hfMCO. Arrow indicates the migration direction. The scale bar represents 5 μm.

See also Figures S6 and S7 and Movies S4, S5, and S6.

we do not exclude potential benefit of adding dissolved Matrigel. We found adding fibroblast growth factor 2 (FGF2) or epidermal growth factor (EGF) is not necessary in our culture system, especially given that SHH signaling promotes progenitor proliferation (Lien et al., 2006). Nevertheless, we did notice that supplementing FGF2 (20 ng/mL) could enhance proliferation of progenitors and consequently the size of organoids (data not shown). Adding FGF2 could be a potential option for cell lines showing lower proliferation rate without exogenous growth factors.

We found hMGEos and hCOs recapitulated transcriptome features of developing human MGE and cortex domains. ATAC-seq confirmed the chromatin re-organization during organoid development in line with the global transcriptional changes. hMGEos and hCOs generate multiple cell types whose identities were delineated by scRNA-seq (Figure 5). Similarly, recent study by Quadrato et al. (2017) demonstrated a production of diverse cell types within organoids related with endogenous classes for cerebral cortex or retina using scRNA-seq. In addition to the well-defined neuronal and neuroprogenitor cell types, we identified metabolically unique intermediate clusters that may represent the neural progenitors in a transition of glycolytic to neural oxidative phosphorylation (Figure 5H). scRNA-seq also distinguished the features of interneurons generated from hMGEo and hCOs. Interneurons from hMGEos maintained the expression of NKX2-1 even after further development, whereas those from hCOs showed no expression of NKX2-1. Difference in developmental timing of oligodendrocyte progenitors and oligodendrocytes was remarkable in late hMGEo and hCO (Figure 5H), validating the concept of oligodendrocyte waves (Kessaris et al., 2006) in a human model.

In parallel with our studies, two groups recently reported methods generating fused ventral and dorsal forebrain organoids as a model of interneuron migration (Bagley et al., 2017; Birey et al., 2017). In all three studies, patterning factors for SHH signaling (e.g., SHH and purmorphamine in our current study and smoothened agonist SAG in Birey et al., 2017 and Bagley et al., 2017) were used to induce ventral fate. The detailed protocols for organoid generation and fusion, however, differ from one another. For instance, Birey et al. (2017) begin with intact hPSC colonies rather than single cells to form the organoids. On the other hand, Bagley et al. (2017) generate organoids from the single cells dissociated from hPSC colonies like our approach. Whereas dual SMAD inhibitors by Birey et al. (2017) and additional Wnt inhibitor by us are used to induce neuroectoderm from hPSCs, Bagley et al. (2017) do not include specific neural induction factors. In forming fused organoids, Bagley et al. (2017) used a single Matrigel droplet to embed two organoids (Bagley et al., 2017), whereas static fusion was applied by us and Birey et al. (2017). Despite these differences, all three groups observed a robust interneuron migration in the fused organoids, which provide an excellent model to study mechanism of human interneuron migration *in vitro*.

Brain organoids have been facilitating our study in brain development and neurological disorders recently. With the rapid progress in organoid techniques, modeling more complex developmental processes by fusing (grafting) different organoids could be promising and may open the field of “next generation” organoid study in the near future.

STAR METHODS

Detailed methods are provided in the online version of this paper and include the following:

- KEY RESOURCES TABLE
- CONTACT FOR REAGENT AND RESOURCE SHARING
- EXPERIMENTAL MODEL AND SUBJECT DETAILS
 - hPSCs culture
- METHOD DETAILS
 - Organoids Culture Conditions
 - Cryosectioning and Immunostaining
 - Real Time Quantitative PCR
 - Dissociation of Organoids
 - Library Preparation for High-throughput Sequencing
 - Data Processing of Bulk RNA-seq and ATAC-seq
 - Data Processing of Single-cell RNA-seq from Chromium System
 - Calcium Imaging
 - Electrophysiological Recordings and Imaging of Biocytin-filled Cells
 - Generation of hfMCOs
 - Live Imaging of hfMCOs
- QUANTIFICATION AND STATISTICAL ANALYSES
- DATA AND SOFTWARE AVAILABILITY

SUPPLEMENTAL INFORMATION

Supplemental Information includes seven figures and six movies and can be found with this article online at <http://dx.doi.org/10.1016/j.stem.2017.07.007>.

AUTHOR CONTRIBUTIONS

Y.X. and I.-H.P. conceived the study. Y.X. established the organoids culture system. Y.X. and N.R. generated and characterized brain organoids. B.C., K.-Y.K., A.P.L., and J.R.N. performed cell culture. Y.X. and B.P. prepared samples for Chromium single-cell RNA-seq. Y.T. performed ATAC-seq and analysis for all the sequencing datasets. Y.-J.K., G.G., S.-M.H., and S.-H.L. performed slice patch-clamp recordings. A.E. and E.G.S. generated and provided HES-3 *NKX2-1*^{GFP/w} reporter line. S.M.W. and M.Z. coordinated and performed deep sequencing. Y.X., Y.T., and I.-H.P. wrote the manuscript.

ACKNOWLEDGMENTS

We thank Dr. Stewart A. Anderson for sharing MGE derivation protocol and Guilin Wang for Chromium service. I.-H.P. was partly supported by NIH (GM0099130-01 and GM111667-01), CSCR (12-SCB-YALE-11 and 13-SCB-YALE-06), KRIBB/KRCF research initiative program (NAP-09-3), and CTSA grant UL1 RR025750 from the National Center for Advancing Translational Science (NCATS), a component of the NIH, and NIH roadmap for Medical Research. This paper's contents are solely the responsibility of the authors and do not necessarily represent the official view of NIH. This work was also supported by the College of Medicine, University of Arkansas for Medical Sciences (startup funding to S.-H.L.) and Core Facilities of the Center for Translational Neuroscience, award P30GM110702, from the IDeA program at NIGMS. A.E. and E.G.S. are supported by research fellowships from the NHMRC (GNT1117596 and GNT1079004). Computation time was provided by Yale University Biomedical High Performance Computing Center.

Received: April 18, 2017

Revised: June 6, 2017

Accepted: July 11, 2017

Published: July 27, 2017

REFERENCES

- Bagley, J.A., Reumann, D., Bian, S., Lévi-Strauss, J., and Knoblich, J.A. (2017). Fused cerebral organoids model interactions between brain regions. *Nat. Methods* 14, 743–751.
- Bellion, A., Baudoin, J.P., Alvarez, C., Bornens, M., and Métin, C. (2005). Nucleokinesis in tangentially migrating neurons comprises two alternating phases: forward migration of the Golgi/centrosome associated with centrosome splitting and myosin contraction at the rear. *J. Neurosci.* 25, 5691–5699.
- Bershteyn, M., Nowakowski, T.J., Pollen, A.A., Di Lullo, E., Nene, A., Wynshaw-Boris, A., and Kriegstein, A.R. (2017). Human iPSC-derived cerebral organoids model cellular features of lissencephaly and reveal prolonged mitosis of outer radial glia. *Cell Stem Cell* 20, 435–449.e4.
- Birey, F., Andersen, J., Makinson, C.D., Islam, S., Wei, W., Huber, N., Fan, H.C., Metzler, K.R.C., Panagiotakos, G., Thom, N., et al. (2017). Assembly of functionally integrated human forebrain spheroids. *Nature* 545, 54–59.
- Buenrostro, J.D., Giresi, P.G., Zaba, L.C., Chang, H.Y., and Greenleaf, W.J. (2013). Transposition of native chromatin for fast and sensitive epigenomic profiling of open chromatin, DNA-binding proteins and nucleosome position. *Nat. Methods* 10, 1213–1218.
- Chambers, S.M., Fasano, C.A., Papapetrou, E.P., Tomishima, M., Sadelain, M., and Studer, L. (2009). Highly efficient neural conversion of human ES and iPS cells by dual inhibition of SMAD signaling. *Nat. Biotechnol.* 27, 275–280.
- Chao, H.T., Chen, H., Samaco, R.C., Xue, M., Chahrour, M., Yoo, J., Neul, J.L., Gong, S., Lu, H.C., Heintz, N., et al. (2010). Dysfunction in GABA signalling mediates autism-like stereotypies and Rett syndrome phenotypes. *Nature* 468, 263–269.
- Darmanis, S., Sloan, S.A., Zhang, Y., Enge, M., Caneda, C., Shuer, L.M., Hayden Gephart, M.G., Barres, B.A., and Quake, S.R. (2015). A survey of human brain transcriptome diversity at the single cell level. *Proc. Natl. Acad. Sci. USA* 112, 7285–7290.
- Falcon, S., and Gentleman, R. (2007). Using GOrilla to test gene lists for GO term association. *Bioinformatics* 23, 257–258.
- Germain, N.D., Banda, E.C., Becker, S., Naegle, J.R., and Grabel, L.B. (2013). Derivation and isolation of NKX2.1-positive basal forebrain progenitors from human embryonic stem cells. *Stem Cells Dev.* 22, 1477–1489.
- Goulburn, A.L., Alden, D., Davis, R.P., Micallef, S.J., Ng, E.S., Yu, Q.C., Lim, S.M., Soh, C.L., Elliott, D.A., Hatzistavrou, T., et al. (2011). A targeted NKX2.1 human embryonic stem cell reporter line enables identification of human basal forebrain derivatives. *Stem Cells* 29, 462–473.
- Hansen, D.V., Lui, J.H., Flandin, P., Yoshikawa, K., Rubenstein, J.L., Alvarez-Buylla, A., and Kriegstein, A.R. (2013). Non-epithelial stem cells and cortical interneuron production in the human ganglionic eminences. *Nat. Neurosci.* 16, 1576–1587.
- Heinz, S., Benner, C., Spann, N., Bertolino, E., Lin, Y.C., Laslo, P., Cheng, J.X., Murre, C., Singh, H., and Glass, C.K. (2010). Simple combinations of lineage-determining transcription factors prime cis-regulatory elements required for macrophage and B cell identities. *Mol. Cell* 38, 576–589.
- Inoue, T., Ota, M., Ogawa, M., Mikoshiba, K., and Aruga, J. (2007). Zic1 and Zic3 regulate medial forebrain development through expansion of neuronal progenitors. *J. Neurosci.* 27, 5461–5473.
- Jo, J., Xiao, Y., Sun, A.X., Cukuroglu, E., Tran, H.D., Göke, J., Tan, Z.Y., Saw, T.Y., Tan, C.P., Lokman, H., et al. (2016). Midbrain-like organoids from human pluripotent stem cells contain functional dopaminergic and neuromelanin-producing neurons. *Cell Stem Cell* 19, 248–257.
- Kadoshima, T., Sakaguchi, H., Nakano, T., Soen, M., Ando, S., Eiraku, M., and Sasai, Y. (2013). Self-organization of axial polarity, inside-out layer pattern, and species-specific progenitor dynamics in human ES cell-derived neocortex. *Proc. Natl. Acad. Sci. USA* 110, 20284–20289.
- Kelava, I., and Lancaster, M.A. (2016). Stem cell models of human brain development. *Cell Stem Cell* 18, 736–748.
- Kessaris, N., Fogarty, M., Iannarelli, P., Grist, M., Wegner, M., and Richardson, W.D. (2006). Competing waves of oligodendrocytes in the forebrain and postnatal elimination of an embryonic lineage. *Nat. Neurosci.* 9, 173–179.
- LaMonica, B.E., Lui, J.H., Hansen, D.V., and Kriegstein, A.R. (2013). Mitotic spindle orientation predicts outer radial glial cell generation in human neocortex. *Nat. Commun.* 4, 1665.
- Lancaster, M.A., and Knoblich, J.A. (2014). Organogenesis in a dish: modeling development and disease using organoid technologies. *Science* 345, 1247125.
- Lancaster, M.A., Renner, M., Martin, C.A., Wenzel, D., Bicknell, L.S., Hurles, M.E., Homfray, T., Penninger, J.M., Jackson, A.P., and Knoblich, J.A. (2013). Cerebral organoids model human brain development and microcephaly. *Nature* 501, 373–379.
- Langmead, B., and Salzberg, S.L. (2012). Fast gapped-read alignment with Bowtie 2. *Nat Methods* 9, 357–359.
- Li, H., Handsaker, B., Wysoker, A., Fennell, T., Ruan, J., Homer, N., Marth, G., Abecasis, G., and Durbin, R.; Subgroup, G.P.D.P. (2009). The Sequence Alignment/Map format and SAMtools. *Bioinformatics* 25, 2078–2079.
- Li, Y., Muffat, J., Omer, A., Bosch, I., Lancaster, M.A., Sur, M., Gehrke, L., Knoblich, J.A., and Jaenisch, R. (2017). Induction of expansion and folding in human cerebral organoids. *Cell Stem Cell* 20, 385–396.e3.
- Lien, W.H., Klezovitch, O., Fernandez, T.E., Delrow, J., and Vasioukhin, V. (2006). alphaE-catenin controls cerebral cortical size by regulating the hedgehog signaling pathway. *Science* 311, 1609–1612.
- Liu, Y., Liu, H., Sauvay, C., Yao, L., Zarnowska, E.D., and Zhang, S.C. (2013). Directed differentiation of forebrain GABA interneurons from human pluripotent stem cells. *Nat. Protoc.* 8, 1670–1679.
- Ma, T., Wang, C., Wang, L., Zhou, X., Tian, M., Zhang, Q., Zhang, Y., Li, J., Liu, Z., Cai, Y., et al. (2013). Subcortical origins of human and monkey neocortical interneurons. *Nat. Neurosci.* 16, 1588–1597.
- Macosko, E.Z., Basu, A., Satija, R., Nemesh, J., Shekhar, K., Goldman, M., Tirosh, I., Bialas, A.R., Kamitaki, N., Martersteck, E.M., et al. (2015). Highly parallel genome-wide expression profiling of individual cells using nanoliter droplets. *Cell* 161, 1202–1214.
- Manuel, M.N., Mi, D., Mason, J.O., and Price, D.J. (2015). Regulation of cerebral cortical neurogenesis by the Pax6 transcription factor. *Front. Cell. Neurosci.* 9, 70.
- Mariani, J., Simonini, M.V., Palejev, D., Tomasini, L., Coppola, G., Szekely, A.M., Horvath, T.L., and Vaccarino, F.M. (2012). Modeling human cortical development in vitro using induced pluripotent stem cells. *Proc. Natl. Acad. Sci. USA* 109, 12770–12775.
- Mariani, J., Coppola, G., Zhang, P., Abyzov, A., Provini, L., Tomasini, L., Amenduni, M., Szekely, A., Palejev, D., Wilson, M., et al. (2015). FOXG1-dependent dysregulation of GABA/glutamate neuron differentiation in autism spectrum disorders. *Cell* 162, 375–390.
- Markram, H., Toledo-Rodriguez, M., Wang, Y., Gupta, A., Silberberg, G., and Wu, C. (2004). Interneurons of the neocortical inhibitory system. *Nat. Rev. Neurosci.* 5, 793–807.
- Maroof, A.M., Keros, S., Tyson, J.A., Ying, S.W., Ganat, Y.M., Merkle, F.T., Liu, B., Goulburn, A., Stanley, E.G., Elefanty, A.G., et al. (2013). Directed differentiation and functional maturation of cortical interneurons from human embryonic stem cells. *Cell Stem Cell* 12, 559–572.
- Melé, M., Ferreira, P.G., Reverter, F., DeLuca, D.S., Monlong, J., Sammeth, M., Young, T.R., Goldmann, J.M., Pervouchine, D.D., Sullivan, T.J., et al.; GTEx Consortium (2015). Human genomics. The human transcriptome across tissues and individuals. *Science* 348, 660–665.
- Mertens, J., Marchetto, M.C., Bardy, C., and Gage, F.H. (2016). Evaluating cell reprogramming, differentiation and conversion technologies in neuroscience. *Nat. Rev. Neurosci.* 17, 424–437.
- Miller, J.A., Ding, S.L., Sunkin, S.M., Smith, K.A., Ng, L., Szafer, A., Ebbert, A., Riley, Z.L., Royall, J.J., Aiona, K., et al. (2014). Transcriptional landscape of the prenatal human brain. *Nature* 508, 199–206.
- Minocha, S., Valloton, D., Ypsilanti, A.R., Fiumelli, H., Allen, E.A., Yanagawa, Y., Marin, O., Chédotal, A., Hornung, J.P., and Lebrand, C. (2015). Nkx2.1-derived

- astrocytes and neurons together with Slit2 are indispensable for anterior commissure formation. *Nat. Commun.* 6, 6887.
- Nicholas, C.R., Chen, J., Tang, Y., Southwell, D.G., Chalmers, N., Vogt, D., Arnold, C.M., Chen, Y.J., Stanley, E.G., Elefanty, A.G., et al. (2013). Functional maturation of hPSC-derived forebrain interneurons requires an extended timeline and mimics human neural development. *Cell Stem Cell* 12, 573–586.
- Paredes, M.F., James, D., Gil-Perotin, S., Kim, H., Cotter, J.A., Ng, C., Sandoval, K., Rowitch, D.H., Xu, D., McQuillen, P.S., et al. (2016). Extensive migration of young neurons into the infant human frontal lobe. *Science* 354, 81.
- Pașca, A.M., Sloan, S.A., Clarke, L.E., Tian, Y., Makinson, C.D., Huber, N., Kim, C.H., Park, J.Y., O'Rourke, N.A., Nguyen, K.D., et al. (2015). Functional cortical neurons and astrocytes from human pluripotent stem cells in 3D culture. *Nat. Methods* 12, 671–678.
- Patel, T.P., Man, K., Firestein, B.L., and Meaney, D.F. (2015). Automated quantification of neuronal networks and single-cell calcium dynamics using calcium imaging. *J. Neurosci. Methods* 243, 26–38.
- Qian, X., Nguyen, H.N., Song, M.M., Hadiono, C., Ogden, S.C., Hammack, C., Yao, B., Hamersky, G.R., Jacob, F., Zhong, C., et al. (2016). Brain-region-specific organoids using mini-bioreactors for modeling ZIKV exposure. *Cell* 165, 1238–1254.
- Quadrato, G., Brown, J., and Arlotta, P. (2016). The promises and challenges of human brain organoids as models of neuropsychiatric disease. *Nat. Med.* 22, 1220–1228.
- Quadrato, G., Nguyen, T., Macosko, E.Z., Sherwood, J.L., Min Yang, S., Berger, D.R., Maria, N., Scholvin, J., Goldman, M., Kinney, J.P., et al. (2017). Cell diversity and network dynamics in photosensitive human brain organoids. *Nature* 545, 48–53.
- Rutherford, L.C., DeWan, A., Lauer, H.M., and Turrigiano, G.G. (1997). Brain-derived neurotrophic factor mediates the activity-dependent regulation of inhibition in neocortical cultures. *J. Neurosci.* 17, 4527–4535.
- Schindelin, J., Arganda-Carreras, I., Frise, E., Kaynig, V., Longair, M., Pietzsch, T., Preibisch, S., Rueden, C., Saalfeld, S., Schmid, B., et al. (2012). Fiji: an open-source platform for biological-image analysis. *Nat. Methods* 9, 676–682.
- Simms, B.A., and Zamponi, G.W. (2014). Neuronal voltage-gated calcium channels: structure, function, and dysfunction. *Neuron* 82, 24–45.
- Subramanian, A., Tamayo, P., Mootha, V.K., Mukherjee, S., Ebert, B.L., Gillette, M.A., Paulovich, A., Pomeroy, S.L., Golub, T.R., Lander, E.S., et al. (2005). Gene set enrichment analysis: a knowledge-based approach for interpreting genome-wide expression profiles. *Proc. Natl. Acad. Sci. U S A* 102, 15545–15550.
- Trapnell, C., Pachter, L., and Salzberg, S.L. (2009). TopHat: discovering splice junctions with RNA-seq. *Bioinformatics* 25, 1105–1111.
- Trapnell, C., Williams, B.A., Pertea, G., Mortazavi, A., Kwan, G., van Baren, M.J., Salzberg, S.L., Wold, B.J., and Pachter, L. (2010). Transcript assembly and quantification by RNA-seq reveals unannotated transcripts and isoform switching during cell differentiation. *Nat. Biotechnol.* 28, 511–515.
- Tyson, J.A., Goldberg, E.M., Maroof, A.M., Xu, Q., Petros, T.J., and Anderson, S.A. (2015). Duration of culture and sonic hedgehog signaling differentially specify PV versus SST cortical interneuron fates from embryonic stem cells. *Development* 142, 1267–1278.
- Wonders, C.P., and Anderson, S.A. (2006). The origin and specification of cortical interneurons. *Nat. Rev. Neurosci.* 7, 687–696.
- Yanagida, M., Miyoshi, R., Toyokuni, R., Zhu, Y., and Murakami, F. (2012). Dynamics of the leading process, nucleus, and Golgi apparatus of migrating cortical interneurons in living mouse embryos. *Proc. Natl. Acad. Sci. USA* 109, 16737–16742.
- Zhang, S.C., Wernig, M., Duncan, I.D., Brüstle, O., and Thomson, J.A. (2001). In vitro differentiation of transplantable neural precursors from human embryonic stem cells. *Nat. Biotechnol.* 19, 1129–1133.
- Zhang, H.M., Chen, H., Liu, W., Liu, H., Gong, J., Wang, H., and Guo, A.Y. (2012). AnimalTFDB: a comprehensive animal transcription factor database. *Nucleic Acids Res.* 40, D144–D149.
- Zhang, Z.N., Freitas, B.C., Qian, H., Lux, J., Acab, A., Trujillo, C.A., Herai, R.H., Nguyen Huu, V.A., Wen, J.H., Joshi-Barr, S., et al. (2016). Layered hydrogels accelerate iPSC-derived neuronal maturation and reveal migration defects caused by MeCP2 dysfunction. *Proc. Natl. Acad. Sci. USA* 113, 3185–3190.
- Zheng, X., Boyer, L., Jin, M., Mertens, J., Kim, Y., Ma, L., Ma, L., Hamm, M., Gage, F.H., and Hunter, T. (2016). Metabolic reprogramming during neuronal differentiation from aerobic glycolysis to neuronal oxidative phosphorylation. *eLife* 5, e13374.
- Zheng, G.X., Terry, J.M., Belgrader, P., Ryvkin, P., Bent, Z.W., Wilson, R., Ziraldo, S.B., Wheeler, T.D., McDermott, G.P., Zhu, J., et al. (2017). Massively parallel digital transcriptional profiling of single cells. *Nat. Commun.* 8, 14049.

STAR★METHODS**KEY RESOURCES TABLE**

REAGENT or RESOURCE	SOURCE	IDENTIFIER
Antibodies		
FOXP1	Abcam	Cat# ab18259
PAX6	DSHB	Cat# AB528427
MAP2	Millipore	Cat# MAB3418
SOX2	Cell Signaling	Cat# 3579
GFAP	Neuromics	Cat# M015052
GFAP	Dako	Cat# Z0334
GFP	Sigma	Cat# SAB4600051
SATB2	Abcam	Cat# ab51502
CTIP2	Cell Signaling	Cat# 12120
NeuN	Cell Signaling	Cat# 24307
Synapsin I	Millipore	Cat# 574777
PSD95	Sigma	Cat# P-246
TBR2	Abcam	Cat# ab23345
N-cadherin	Santa Cruz	Cat# sc-8424
DLX2	Abcam	Cat# ab135620
Ascl1	Neuromics	Cat# MO15048
β-Tubulin III	Sigma	Cat# T8578
GABA	Sigma	Cat# A0310
vGAT	Synaptic Systems	Cat# 131003
Gephyrin	Synaptic Systems	Cat# 147001
Somatostatin	Millipore	Cat# MAB354
CXCR4	Abcam	Cat# ab181020
Neuropilin 1	Abcam	Cat# ab81321
FAM107A	Sigma	Cat# HPA055888
Olig1	Santa Cruz	Cat# sc-373679
Reelin	MBL	Cat# D223-3
phospho-Histone H3 (Ser10)	Millipore	Cat# 06-570
Chemicals, Peptides, and Recombinant Proteins		
mTeSR1	Stem Cell Technologies	Cat# 05875
DMEM/F12	Life Technologies	Cat# 11330057
Neurobasal Medium	Life Technologies	Cat# 2110349
Amino acids, non-essential	Life Technologies	Cat# 11140050
Penicillin/Streptomycin	Life Technologies	Cat# 15140-122
Glutamax	Life Technologies	Cat# 35050
β-Mercaptoethanol	Sigma	Cat# M7522
N2	Life Technologies	Cat# 17502-048
B27	Life Technologies	Cat# 17504-044
B27 supplement without vitamin A	Life Technologies	Cat# 12587010
KnockOut Serum Replacement	Life Technologies	Cat# 10828-028
Matriigel	BD	Cat# 354230
Y-27632	Stem Cell Technologies	Cat# 72304
Dispase (100 ml)	Stem Cell Technologies	Cat# 07913
Accutase (100 ml)	Stem Cell Technologies	Cat# AT104
FBS	Life Technologies	Cat# 10437028

(Continued on next page)

Continued

REAGENT or RESOURCE	SOURCE	IDENTIFIER
LDN-193189	Sigma	Cat# SML0559
SB431542	Abcam	Cat# ab120163
XAV939	Sigma	Cat# X3004
SHH	R&D Systems	Cat# 464-SH-200
purmorphamine	Stem Cell Biotech	Cat# 72204
BDNF	Prepotech	Cat# 450-02
cAMP	Millipore	Cat# 28745
Ascorbic acid	Sigma	Cat# A92902
Bicuculline	Sigma	Cat# 14343
TTX	Abcam	Cat# ab120054
Blebbistatin	Abcam	Cat# ab120425
O.C.T. compound	Tissue-Tek	Cat# 4583
Bovine serum albumin	American Bioanalytical	Cat# AB01088
ProLong Gold Antifade Reagent	ThermoFisher	Cat# P36930
Biocytin	Sigma	Cat #B4261
Alexa Fluor 594 Streptavidin	Jackson ImmunoResearch	Cat # 016-580-084
Critical Commercial Assays		
Papain Dissociation System	Worthington Biochemical Corporation	Cat# LK003150
RNeasy mini kit	QIAGEN	Cat# 74104
RNase-Free DNase Set	QIAGEN	Cat# 79254
iScript cDNA synthesis kit	Biorad	Cat# 1708891
SsoFast EvaGreen Supermix	Biorad	Cat# 1725201
Single Cell 3' Reagent Kits	10x GENOMICS	
Nextera DNA Library Prep Kit	Illumina	Cat# FC-121-1030
EinElute kit	QIAGEN	Cat# 28004
High Fidelity 2xPCR master mix	NEB	Cat# M0541S
AxyPrepTM Mag PCR Clean-up kit	AXYGEN	Cat# 14-223-153
Deposited Data		
Raw and proposed RNA-seq and ATAC-seq	This paper	GEO: GSE97882
Human genome assembly hg19	N/A	https://genome.ucsc.edu/
RNA-seq for <i>in vivo</i> embryonic brain regions	BrainSpan	http://www.brainspan.org/
scRNA-seq for fetal and adult brains	Darmanis et al., 2015	SRA: SRP057196
Experimental Models: Cell Lines		
HES-3 <i>NKX2-1</i> ^{GFP/w}	Elefanten lab	https://www.ncbi.nlm.nih.gov/pubmed/21425409
H1 hESC line	WiCell	https://www.ncbi.nlm.nih.gov/pubmed/9804556/
Human iPSC line 1090	This paper	
Recombinant DNA		
AAV1.syn.GCaMP6s.WPRE.SV40	Penn Vector Core	AV-1-PV2824
pLV-hSyn-RFP	Addgene	https://www.addgene.org/22909/
Software and Algorithms		
Tophat (v2.0.12)	Trapnell et al., 2009	https://ccb.jhu.edu/software/tophat/index.shtml
Samtools (v1.3.1)	Li et al., 2009	http://samtools.sourceforge.net/
Bowtie (v2.2.9)	Langmead and Salzberg, 2012	http://bowtie-bio.sourceforge.net/bowtie2/index.shtml
Cufflinks (v1.2.1)	Trapnell et al., 2010	http://cole-trapnell-lab.github.io/cufflinks/
GSEA (v2.2.2)	Subramanian et al., 2005	http://software.broadinstitute.org/gsea/index.jsp
Cellranger (v1.3.0)	N/A	https://support.10xgenomics.com/
CellrangerRkit (v1.1.0)	N/A	https://support.10xgenomics.com/
Seurat (v1.4.0.14)	Macosko et al., 2015	http://satijalab.org/seurat/

(Continued on next page)

Continued

REAGENT or RESOURCE	SOURCE	IDENTIFIER
HOMER (v4.9)	Heinz et al., 2010	http://homer.salk.edu/homer/index.html
GOstats (v3.4)	Falcon and Gentleman, 2007	https://www.bioconductor.org/packages/release/bioc/html/GOstats.html
igraph (v1.0.1)	N/A	http://igraph.org/redirect.html
pyDNase (v0.2.4)	N/A	http://pythonhosted.org/pyDNase/
R (v3.3.2)	N/A	https://www.r-project.org/
Qcapture Pro7 software	QICAM	https://www.qimaging.com/resources/pdfs/QCaptureProManual.pdf
MATLAB	MathWorks	https://www.mathworks.com/products/matlab.html
FluoroSNNAP	N/A	http://www.seas.upenn.edu/~molneuro/fluorosnap.html
Fiji	N/A	https://fiji.sc
Clampfit 10	Molecular Devices	
Other		
U-bottom ultra-low-attachment 96-well plate	Corning	CLS7007-24EA
Ultra-low-attachment 6-well plate	Corning	CLS3471-24EA
Orbital shaker	IKA	KS260

CONTACT FOR REAGENT AND RESOURCE SHARING

Further information and requests for reagents may be directed to, and will be fulfilled by, the lead contact, Dr. In-Hyun Park (inhyun.park@yale.edu).

EXPERIMENTAL MODEL AND SUBJECT DETAILS**hPSCs culture**

HES-3 *NKX2-1*^{GFP/w} and H1 human ES cells, and human iPSC (1090) were maintained in feeder-free culture condition. iPSC line 1090 was derived from peripheral blood mononuclear cell of a male donor by overexpressing the reprogramming factors OCT4, SOX2, KLF4, and MYC through Sendai virus vectors, and the pluripotency was confirmed (Figures S5A and S5B). hPSCs were cultured on Matrigel coated cell culture dish with mTeSR1 media, and were passaged every 7 days by Dispase (0.83 U/ml) treatment. All experiments involving hESCs and hiPSCs were approved by the Yale Embryonic Stem Cell Research Oversight Committee (ESCRO), and IRB.

METHOD DETAILS**Organoids Culture Conditions**

On day 0 of organoid culture, any pre-differentiated cells in the hPSCs culture were removed by scraping under microscope and ESC or iPSC colonies were dissociated into single cell suspension with Accutase. 9,000 cells were then plated into each well of a U-bottom ultra-low-attachment 96-well plate in neural induction media supplemented with 50 µM Y-27632 compound and 5% (v/v) heat-inactivated FBS. Neural induction media contained DMEM-F12, 15% (v/v) knockout serum replacement, 1% (v/v) MEM-NEAA, 1% (v/v) Glutamax, 100 µM β-Mercaptoethanol, 100 nM LDN-193189, 10 µM SB431542, and 2 µM XAV939. Media was replenished every other day until day 10. On day 2, neural induction media was supplemented with 50 µM Y-27632 compound without heat-inactivated FBS. From day 4, Y-27632 compound was no longer supplemented. From day 0 to day 10, cell aggregates in the ultra-low-attachment 96-well plate were cultured statically in 37° incubator with 5% CO₂.

After 10 day stationary culture, organoids in 96-well plate were transferred to ultra-low-attachment 6-well plate. Maximum 8 organoids were transferred into each well of the 6-well plate. To generate hMGEOs, ventral patterning media was used from day 10 to day 18, with media change every other day. The ventral patterning media contained DMEM-F12, 0.15% (w/v) Detrose, 100 µM β-Mercaptoethanol, 1% (v/v) N2 supplement, 2% B27 supplement without vitamin A, 100 ng/ml recombinant SHH, and 1 µM purmorphamine. To generate hCOs, neural differentiation media without vitamin A was used from day 10 to day 18. The media contained 1:1 mixture of DMEM-F12 media and Neurobasal media, supplemented with 0.5% (v/v) N2 supplement, 1% (v/v) B27 supplement without vitamin A, 1% (v/v) Glutamax, 0.5% (v/v) MEM-NEAA, 0.025% (v/v) human insulin solution, 50 µM β-Mercaptoethanol, and 1% (v/v) Penicillin/Streptomycin. Cell culture plate was kept on orbital shaker with speed of 80 rpm/min, and media was replenished every other day.

From day 18, for both hMGEos and hCOs, neural differentiation media with vitamin A was used and replenished every 4 days. The media components were the same with the neural differentiation media used for hCOs between day 10 to day 18 described above, except that B27 supplement with vitamin A was used. In addition, 20 ng/ml BDNF, 200 μ M cAMP, and 200 μ M ascorbic acid were supplemented to the media. For the majority of the experiments in the current study, HES-3 *NKX2-1*^{GFP/w} cells were used unless otherwise stated in the results.

Cryosectioning and Immunostaining

Organoids were fixed in 4% paraformaldehyde (PFA) at 4°C for 15 min, washed 3 times with PBS (10 min incubation at RT for each wash), and transferred to 30% sucrose solution for incubation overnight at 4°C. Sucrose solution was then removed and organoids were equilibrated with O.C.T compound at RT for 15 min. Organoids were then transferred to tissue base molds and embedded within O.C.T compound on dry ice. Organoids blocks were then stored at -80°C or used for cryosectioning to obtain 40 μ m slices. Cryosection was washed with PBS, incubated with 0.1% Triton-100 for 15 min at RT, blocked with 3% bovine serum albumin for 2 hr at RT, and then incubated with primary antibody diluted in 3% BSA overnight at 4°C. After washed with PBS, cryosection was incubated with secondary antibody diluted in 3% BSA for 1 hr at RT. Alexa Fluor Dyes were used at 1:1000 dilution and nuclei were stained by DAPI. After staining, cryosection was mounted with ProLong Gold Antifade Reagent and imaged with Leica TCS SP5 confocal microscope.

Real Time Quantitative PCR

Total RNA samples were isolated from the whole organoids using the RNeasy Mini Kit. 1 μ g of RNA was used to generated cDNA using the iScript Select cDNA Synthesis Kit. Real time quantitative PCR was performed using the SsoFast EvaGreen Supermix in the CFX96 Real-Time PCR System. The PCR cycling conditions were: 95°C for 15 min, followed by 40 two-step cycles at 94°C for 10 s and 60°C for 45 s. Primers used were as follows: NKX2-1 forward: 5'-GAGTCCAGAGCCATGTCAGC-3', reverse: 5'-GCATAAAACAGCTTGGGTGT-3'; SST forward: 5'-GCTGCTGCTGAACCCAAC-3', reverse: 5'-CGTTCTCGGGTGCCATAG-3'; PV forward: 5'-AAAGAGTGCAGATGTGAAG-3', reverse: 5'-ACCCCAATTGCGTCCC-3'; NPY forward: 5'-CGCTGCGACAC TACATCAC-3', reverse: 5'-CAGGGTCTTCAAGCCGAGTT-3'; CALB forward: 5'-TCCAAGCAGTAGACATGCTGTT-3', reverse: 5'-ACAACCATACTGTCCCACA-3'.

Dissociation of Organoids

For early stage organoids that were cultured less than 1 month, dissociation was performed by using Accutase. Organoids were washed once with Hank's Balanced Salt Solution, then incubated with Accutase in 37°C water bath for 20 min. Accutase was then removed and organoids were washed 3 times with HBSS. Gentle trituration was performed to obtain single cell suspension. For dissociation of older organoids, hMGEos or hCOs were dissociated using the papain dissociation system according to the instructions from the manufacturer. All the solutions used were oxygenated for 5 min with 95% O₂:5% CO₂ to improve cell viability. Briefly, organoids were washed once with HBSS, then quickly dissected into small pieces in oxygenated papain solution. After dissection, the tissue suspension was re-equilibrated with 95% O₂:5% CO₂, and incubated in 37°C water bath for 60 min. The suspension was gently shaken every 20 min during the incubation period. Then gentle trituration was performed to obtain single cell suspension and papain was inactivated with albumin-ovomucoid inhibitor solution.

Library Preparation for High-throughput Sequencing

For bulk RNA-seq, total RNA samples were isolated from ESCs or whole organoid samples using the RNeasy Mini Kit. hMGEos or hCOs were collected from different culture wells and combined for RNA isolation after 30 (12 hMGEos and 11 hCOs) and 72 (8 hMGEos and 8 hCOs) days of culture. Libraries were constructed using Tru-Seq RNA library preparation kits, followed by sequencing in HiSeq 2000 with manufacture's protocol.

For single cell RNA sequencing, hMGEos or hCOs were collected from different culture wells, combined, and dissociated into single cells (early stage group-1 (day 30): 8 hMGEos and 8 hCOs; early stage group-2 (day 30): 12 hMGEos and 10 hCOs; late stage group-1 (day 72): 7 hMGEos and 8 hCOs; late stage group-2 (day 79): 11 hMGEos and 10 hCOs). Cells dissociated from organoids were suspended in 1% BSA/PBS + 10 μ M Y27632 and stained with propidium iodide (PI) for 15 min on ice. PI-negative cells were collected by FACS and re-suspended in 0.04% BSA/PBS at a concentration of 128 cells/uL to generate cDNA libraries with the Single Cell 3' Reagent Kits, according to the manufacturer's instructions. Briefly, cells were partitioned into nanoliter-scale Gel Bead-In-Emulsions (GEMs). Using microfluidics, cells were flowed at a limiting dilution into a stream of Single Cell 3' Gel Beads and then a stream of oil. This ideally encapsulates a single cell and an individual gel bead in an oil suspension. Upon cell lysis and dissolution of the Single Cell 3' Gel Bead within the droplet, primers containing an Illumina P7 and R2 sequence, a 14 bp 10xBarcode, a 10 bp randomer, and a poly-dT primer sequence were released and mixed with the cell lysate and bead-derived Master Mix. Barcoded, full-length cDNA from poly-adenylated mRNA was then generated in each individual bead. After this, the individual droplets were broken and homogenized before the remaining non-cDNA components were removed with silane magnetic beads. The libraries were then size-selected, and the R2, P5, and P7 sequences were added to each selected cDNA during end repair and adaptor ligation. After Illumina bridge amplification of the cDNA, each library was sequenced using the Illumina HiSeq4000 2x150bp in Rapid Run Mode.

ATAC-seq library was prepared as described in a previous report (Buenrostro et al., 2013). *NKX2-1*^{GFP/w} ESCs and 72 day old organoids (8 hMGEos and 8 hCOs from individual culture wells) were dissociated into single cells. 50,000 cells from each group were lysed by cold lysis buffer (10mM Tris-HCl, pH7.4, 10mM NaCl, 3mM MgCl₂, 0.1% IGEPAL CA-630). After spinning at 500 g for 5min, the pellet was used for transposition reaction by Nextera® DNA Library Prep Kit. Following purification by QIAGEN EinElute kit, ATAC-seq library was constructed and amplified by NEB High Fidelity 2xPCR master mix. Finally, the library was purified by AxyPrepTM Mag PCR Clean-up kit.

Data Processing of Bulk RNA-seq and ATAC-seq

Human genomic sequences and RefSeq gene coordinates (version hg19) were obtained from UCSC. All RNA-seq reads were mapped to human genome by Tophat2 (v2.0.12) (Trapnell et al., 2009). Relative expression level (RPKM value) was then calculated by Cufflinks (v1.2.1) using Refseq genes as reference annotation with “–GTF” option (Trapnell et al., 2010). Differentially-expressed genes in organoids to their parental hESCs were defined by 2-fold change (Figures 4B and 4C). GO analysis was then performed to the differentially-expressed genes by GOstats (v2.24.0) in Bioconductor. False discovery rate (FDR) was calculated to each GO term by Benjamini-Hochberg method with p.adjust function in R. GO terms with FDR < 0.05 were used as statistical significance.

The list of tissue-specific genes was obtained from (Melé et al., 2015). Transcriptome profiles of all available brain regions in 8 and 9 pcw were downloaded from BrainSpan database (<http://www.brainspan.org/>). Genes with more than 2 fold change and t test p < 0.05 were used as gene signatures of each in vivo brain region. Enrichment of these gene sets were evaluated by Gene Set Enrichment Analysis (GSEA) software (v2.2.2) with 1,000 permutations of gene sets, weighted enrichment statistic and signal-to-noise separation metric (Figures 4A and 4D).

We mapped ATAC-seq reads to hg19 human genome by Bowtie2 software (v2.2.9) with options “–local -D 15 -R 3 -N 1 -L 20 -S,1,0.50 -k 1.” Reads with their mates were mapped in the same chromosome and their insert sizes were less than nucleosome size (= 150bp) was retained for the identification of open chromatin regions. To identify Tn5 hypersensitive sites (THSs), peak calling was performed by findPeak in HOMER software (v4.9) with “–localSize 50000 -size 100 -minDist 50 -fragLength 0 -o auto.” ΔTHS score was calculated with all pairwise comparison of ESC, hCO and hMGEo by dnase_ddhs_scorer.py script with “-A” option in pyDNase library (v0.2.4) (Figure S2). ATAC-seq peaks with more than four ΔTHS score were defined as unique dOCRs to each stage. Wilcoxon rank-sum test was performed by comparing expression ratio (log₂(ratio)) of target and non-target genes of dOCRs to evaluate enrichment of dOCRs. GO analysis was performed to genes, whose distance from dOCRs was less than 10kbp (Figure 4F).

Data Processing of Single-cell RNA-seq from Chromium System

Mapping to hg19 human genome, quality control and read counting of Ensembl genes was performed by cellranger software with default parameter (v1.3.0) (Figure S3A). Data visualization was performed by cellrangerRKit (v1.1.0). Normalization, dimensionality reduction and clustering of single cells were performed by Seurat (v 1.4.0.14) in Bioconductor (Macosko et al., 2015). Briefly, read count was first normalized per cell and transformed to log₂ scale by Setup function. Cells with more than 200 genes and genes detected in more than 3 cells were retained for subsequent analyses. Negative-binomial regression was then performed to variable genes (more than zero dispersion) using batch and UMI as confounding variables. Principal component analysis was conducted using the regressed variable genes by PCAFast function in Seurat package with “pcs.compute=20” parameter. Using top five principal components (singular value > 1,000), we reduced the dimensionality by t-Distributed Stochastic Neighbor Embedding (tSNE). Cells were then grouped by a shared nearest neighbor modularity optimization using FindClusters function with four resolution value. To compare transcriptional similarity of clusters, classification tree was constructed based on average expression of the set of variable genes. Internal nodes of the tree were assessed by the out of bag error (OOBE) from random forest classifier. Transcriptionally-similar clusters were merged by selecting internal nodes with more than 0.2 OOBE. Furthermore, differentially-expressed genes were identified with all pairwise comparisons of clusters. Clusters with less than five differentially-expressed genes (> 1.5 fold and t test p-value < 0.05) were merged. Each cluster was characterized according to unique marker expression and its significant GO terms (Figures S3G and S4A). Clusters with the same annotation were plotted by the same color in Figure 5C.

Systematic errors, including doublet, mapping bias or batch effect, confound downstream analysis of single-cell transcriptome and thus should be removed prior to analysis (Zheng et al., 2017). Doublet frequency in our scRNA-seq were evaluated by counting cells expressing TBR1 or GFAP, which were exclusively expressed in cortical excitatory neuron (referred to as cortical neuron, CN) and astrocyte, respectively (Figure S3C). Mapping ratio and total UMIs were calculated in individual cells, and their biases among clusters were also compared (Figure S4A). Batch effect after Seurat normalization was evaluated between two biological replicates. We calculated Euclidean distances of data point pairs within one replicate or between two replicates. 1,000 pairs were randomly selected from the within group and the between group, and their distances were compared by Wilcoxon rank-sum test (Figure S3B).

Cells within IN1-5 cluster from hMGEos and hCOs were compared to identify the difference between hMGEo- and hCO-derived interneurons by t test (Figure S5G).

The gene list for transcriptional and epigenetic regulatory factors were obtained from AnimalTFDB v2.0 (Zhang et al., 2012). After removing regulatory factors not expressed in any cells, we calculated Pearson correlation coefficient with all pairwise comparison. The co-expressed network of regulatory factors was constructed by connecting them with more than 0.125 correlation coefficient. Transcription factors were grouped using edge.betweenness.community function and network graph was drawn by graph.adjacency function in igraph R package (v1.0.1) (Figure 5J). Public RNA-seq data by C1 Fluidigm system from human fetal and adult

healthy cortex were downloaded from NCBI Short Read Archive (SRP057196) (Darmanis et al., 2015). As shown above, mapping and calculation of gene expression level were performed by Tophat2 and Cufflinks software, respectively. Gene signatures of NPC and newly born neuron were obtained by 4-fold change and t test p value < 0.05 between replicating and quiescent neuron (Figure S4B). Gene signatures for AS, OL and OPC were obtained by comparing each cell type to the other cells with the same threshold (Figure S4E).

Calcium Imaging

hMGEos and hCOs derived from H1 hESCs and hiPSC (1090) were used for calcium imaging, respectively. Organoids were transduced with AAV1.syn.GCaMP6s.WPRE.SV40 (Penn Vector Core) and 10~15 days after transduction intact organoids were used for calcium imaging. Nikon inverted microscope (Eclipse TS100) was used to observe calcium surges with 10X (area-scale) or 20X (single cell level) objectives at 488-nm excitation. Time lapse images were captured using a Digital CCD camera (QICAM: FAST 1394) and Qcapture Pro7 software (QICAM) at a speed of 1 frame/sec (FPS). For chemical treatment, images were obtained in the same location before and 10 min after adding either TTX (1 μ M) or bicuculline (50 μ M). Tracings of single cell calcium surges were analyzed using MATLAB software with FluoroSNAP code (Patel et al., 2015). Area-scale image series were analyzed using Fiji software (Schindelin et al., 2012).

Electrophysiological Recordings and Imaging of Biocytin-filled Cells

Organoids were embedded in a 4% agarose block. Slices (250 μ m) were cut in chilled oxygenated (95% O₂/5% CO₂) sucrose solution containing (in mM: 85 NaCl, 75 sucrose, 2.5 KCl, 25 glucose, 1.25 NaH₂PO₄, 4 MgCl₂, 0.5 CaCl₂, and 24 NaHCO₃) using Vibratome slicer (Leica 1200S). After 1 hr incubation in oxygenated sucrose solution at 33°C, electrophysiological recordings were obtained using artificial cerebrospinal fluid (ACSF) containing (in mM: 126 NaCl, 2.5 KCl, 26 NaHCO₃, 2 CaCl₂, 2 MgCl₂, 1.25 NaH₂PO₄, and 10 glucose). Individual cells were visualized with an upright microscope (Nikon Eclipse FN1) with infrared differential interference contrast optics with 60X objective. Whole-cell patch-clamp recordings were obtained from individual cells with borosilicate glass pipettes (5–7 M Ω) when filled with internal solution containing 126 mM K-gluconate, 4 mM KCl, 10 mM HEPES, 4 mM ATP-Mg, 0.3 mM GTP-Na, 10 mM phosphocreatine, and 0.5% biocytin with a pH 7.2, and osmolality of 290 mOsm. During recordings, slices were continuously perfused with oxygenated (95% O₂/5% CO₂) ACSF at the rate of 2.5 ml/min. Recordings were obtained using MultiClamp700B amplifiers (Molecular Devices), filtered at 3 kHz using a Bessel filter and digitized at 10 kHz with Digidata 1440A digitizer (Molecular Devices). In order to characterize electrophysiological properties, cells were injected with hyperpolarizing and depolarizing square wave current pulses (−5 to +25 pA, 5 pA increment, 1 s). The data were analyzed using the Clampfit 10 software (Molecular Devices).

After the recordings, organoid slices were transferred into a fixative solution containing 4% paraformaldehyde and 0.2% picric acid in 0.1M phosphate buffer for 24 hr, and subsequently stained with Alexa Fluor 594 Streptavidin (Jackson ImmunoResearch; 1:500) to detect biocytin. Slices were mounted in Vectashield Medium (Vector Laboratories) and subjected to Z stack image acquisitions using Nikon C1 confocal microscope (objective: 40x/1.3, Plan Fluor).

Generation of hfMCOs

After various trials of fusion strategies, we found spontaneous fusion of two closely-positioned hMGEo and hCO was the most efficient and convenient approach. Briefly, on day 18 of organoids culture, single hMGEo and single hCO were transferred into one well of ultra-low-attachment 96-well plate and cultured statically for 3 days to allow spontaneous fusion sufficiently. Half of the neural differentiation media was carefully changed 2 days after fusion, without agitating the organoids on the bottom. 3 days later, the fused organoids (hfMCOs) were transferred to ultra-low-attachment 6-well plate for spinning culture, and the following culture conditions were the same with cultures of hMGEos and hCOs. To generate hfMCOs for neuronal calcium imaging, H1 hESCs-derived hMGEos and hCOs were incubated with media containing AAV1.syn.GCaMP6s.WPRE.SV40 and Lenti-hSyn-RFP virus overnight, respectively. The next day, Gcamp6s-labeled hMGEos and RFP-labeled hCOs were fused as described above.

Live Imaging of hfMCOs

Live images were captured in hfMCOs on the hCO side 2 weeks after fusion using the Leica TCS SP5 confocal microscope with 63x objective. The microscope was equipped with a controlled cell culture chamber, which was set up to keep 37°C temperature and 5% CO₂ in the environment during live imaging. A x, y, z, t scanning mode was used to obtain z stack images for 10–12 hr with 10 min time interval. 4-D reconstruction of the images was then performed using Leica LAS-X software. For myosin II inhibition assay, hfMCOs that showed efficient migration of NKX2-1-GFP⁺ cells on hCO side were treated with 50 μ M blebbistatin, equilibrated for 30 min in 37° spinning culture incubator with 5% CO₂, and then live imaging was performed as described above. Quantification of neuron migration was performed using Leica LAS-X software. Only focus planes clearly capturing somas were used, and migrating speed was calculated as follow: speed = distance of soma translocation (μ m)/[(F2-F1)x10 (min)], in which F2 and F1 represented the frame number after and before soma translocation happened. % of migrating neurons was calculated by dividing the number of translocating somas by total soma numbers within the focus plane. The ratio of active growth cone was calculated by dividing numbers of forward moving growth cones by total soma numbers within the focus plane.

QUANTIFICATION AND STATISTICAL ANALYSES

For quantification of immunostaining, qPCR, and migration assay, unpaired t test was used to determine the statistical significance. For processing of high-throughput sequencing data, please refer to their method descriptions for details of statistical method used for specific analysis. The statistical details of experiments can also be found in the figure legends and related results.

DATA AND SOFTWARE AVAILABILITY

The accession number of data generated in this study is GEO: GSE97882.

Supplemental Information

**Fusion of Regionally Specified hPSC-Derived
Organoids Models Human Brain Development
and Interneuron Migration**

Yangfei Xiang, Yoshiaki Tanaka, Benjamin Patterson, Young-Jin Kang, Gubbi Govindaiah, Naomi Roselaar, Bilal Cakir, Kun-Yong Kim, Adam P. Lombroso, Sung-Min Hwang, Mei Zhong, Edouard G. Stanley, Andrew G. Elefantiy, Janice R. Naegele, Sang-Hun Lee, Sherman M. Weissman, and In-Hyun Park

Supplemental Figure Legends

Figure S1. Characterization of hMGEOS. Related to Figure 1.

(A-C) Staining for GFP, PAX6, SOX2, and GFAP in cells dissociated from hMGEOS. Cells are dissociated from 20 day old organoids and are further cultured for 1 day before staining. In (C), GFAP are found to be expressed in *NKX2-1-GFP*⁻ cells (arrow) or *NKX2-1-GFP*⁺ cells without typical neuronal morphology (arrow head). Mean \pm SD for hMGEOS (n=10) are shown. Scale bar, 25 μ m.

(D) Staining for GFP and ASCL1 in cryosection of 71 day old hMGEOS. Scale bar, 20 μ m.

(E) Quantitative RT-PCR assay of PV, NPY, and CALB expression from hMGEOS exposed to various doses of SHH. Mean \pm SD are shown for each condition (n=4). ***, $P<0.001$; **, $P<0.01$; *, $P<0.05$.

(F and G) Migration streams inside 75 day old hMGEOS. Arrows show migrating directions, which are directed towards or parallel to the surface. Note a core with less viable cells indicated in K. Scale bar, 50 μ m in K, 25 μ m in L.

(H and I) A core enriched with cell death is shown in 75 days old hMGEOS (M), where extensive DLX+ cells could still be detected (N). Scale bar, 50 μ m in M, 25 μ m in N.

Figure S2. Histogram of Δ Tn5 Hypersensitive Site (THS) score between organoids and ESCs or between hCOs and hMGEOS. Related to Figure 4.

Dashed lines represent -4 and 4 Δ THS score. Count of dOCRs was shown.

Figure S3. Clustering and Dissection of Single-cell RNA-seq Data. Related to Figure 5.

(A) Statistics of single-cell RNA-seq.

(B) Batch effects of two biological replicates evaluated by Euclidean distance of randomly-selected data point pairs within and between replicates.

(C) Expression pattern of GFAP and TBR1 at single-cell level. X and Y axis represents UMIs of GFAP and TBR1, respectively. Cells with reads mapped only in GFAP were colored by red; Cells only in TBR1 were by green; Cells in both GFAP and TBR1 were by blue; Cells without any reads in GFAP and TBR1 were by black.

(D) tSNE plot of single-cell transcriptome distinguished by 29 different clusters.

(E) Cell variability among replicates in all clusters. Cells from each replicate were distinguished by colors.

(F) Expression patterns of genes related with early neurogenesis and neuronal growth cone.

(G) Schematic representation of cluster annotation.

Figure S4. Expression Patterns of Lineage-specific Genes. Related to Figure 5.

- (A) Mapping ratio, total UMI counts and GO analysis for 29 clusters. Mean \pm S.D. of mapping ratio and total UMI per cell in each cluster were shown in upper panel. In bottom panel, $-\log_{10}(\text{FDR})$ of GO terms was shown by red color.
- (B) Enrichment of gene signatures for NPC and newly born neuron. Enrichment and depletion are scaled by $-\log_{10}(\text{FDR})$ and shown by red and blue colors, respectively.
- (C) Expression patterns of gene related to pluripotency.
- (D) Co-expression pattern of TBR2, TBR1, and VIM at single cell level.
- (E) Enrichment of gene signatures for AS, NPC and OL.
- (F) Expression patterns of key transcription factors among 29 clusters. Mean \pm S.E.M. of Log₂(normalized read count) are plotted by bargraph.

Figure S5. Activity and Synaptogenesis in hCOs. Related to Figure 6.

- (A) Immunostaining for pluripotent markers OCT4 and SSEA-3 in iPSC line 101090. Scale bar, 50 μm .
- (B) Flow cytometry analysis of SSEA-4+ cells in iPSC line 101090.
- (C) Calcium imaging of intact 45 day old hCOs. Region of interest (ROI) shows cells expressing hsyn-GCaMP6s and undergoing calcium surges (Left). Right side shows time-lapse calcium surges of ROIs, which can be blocked by adding TTX (1 μM). Scale bar, 50 μm .
- (D) Representative imaging showing synchronization of calcium surges after bicuculline disinhibition. Calcium imaging is performed in intact 45 day old hCOs before and 10 min after bicuculline (50 μM) treatment. Scale bar, 50 μm .
- (E) Staining for pre-synaptic protein SYN1 and post-synaptic protein PSD95 in sections of 46 day old hCOs. Scale bar, 5 μm .

Figure S6. Migration Behaviors in hMGEOs and hCOs Cultures. Related to Figure 7.

- (A) Schematic view of Matrigel embedding stage during hMGEOs culture. On day 10, organoids are individually embedded in Matrigel droplet and subjected to further culture as described in Figure 1A. Scale bar, 125 μm .
- (B) Images showing neurons that migrate out from hMGEOs into Matrigel matrix during culture. Scale bar, 125 μm .
- (C) 27 days after Matrigel embedding, neurons from hMGEOs almost occupied the whole Matrigel matrix. Scale bar, 125 μm .

- (D) Images showing *NKX2-1-GFP*⁺ cells on the surface of embedding Matrigel 27 days after embedding. Scale bar, 125 μm .
- (E) Image showing cells from hCOs that also migrated out into Matrigel after embedding on day 10. Scale bar, 125 μm .
- (F) hMGEo derived from HES-3 *NKX2.1*^{GFP/W} and H1 lines were fused and then separated (left). After another 3 day culture, *NKX2-1-GFP*⁺ cells were observed interior of H1-derived hMGEos. Scale bar, 50 μm .

Figure S7. Migration Behaviors in hfMCOs. Related to Figure 7.

- (A) Immunostaining for GFP and SOX2 in sections of hfMCOs 14 days post fusion (dpf). Note migration streams are largely excluded outside of VZ-like areas. Scale bar, 50 μm .
- (B) Image showing inefficient migration where MGE side encounter less developed and superficially located cortical VZ-like areas. Arrows show directions of migration stream, which is diverted towards interior of hCO. Sectioning and staining are performed 14 dpf. Scale bar, 50 μm .
- (C) Inside hCO, *NKX2-1-GFP*⁺ cells still showed migration pattern that is confined outside of VZ-like areas. Sectioning and staining are performed 14 dpf. Scale bar, 25 μm .
- (D) The fusion border in hfMCOs shows efficient cell migration from hMGEo side to hCO side without treatment (left, 6 out of 9 hfMCOs showed migration), whereas in the presence of 70 μM blebbistatin cell migration is completely blocked (Right, 0 out of 4 showed migration). Images are taken 6 dpf. Scale bar, 20 μm .
- (E) Immunostaining for vGAT and GFP in sections of hfMCOs at 21dpf reveals neurons migrating to hCOs side maintain their GABAergic identity. Scale bar, 20 μm .

Figure S1

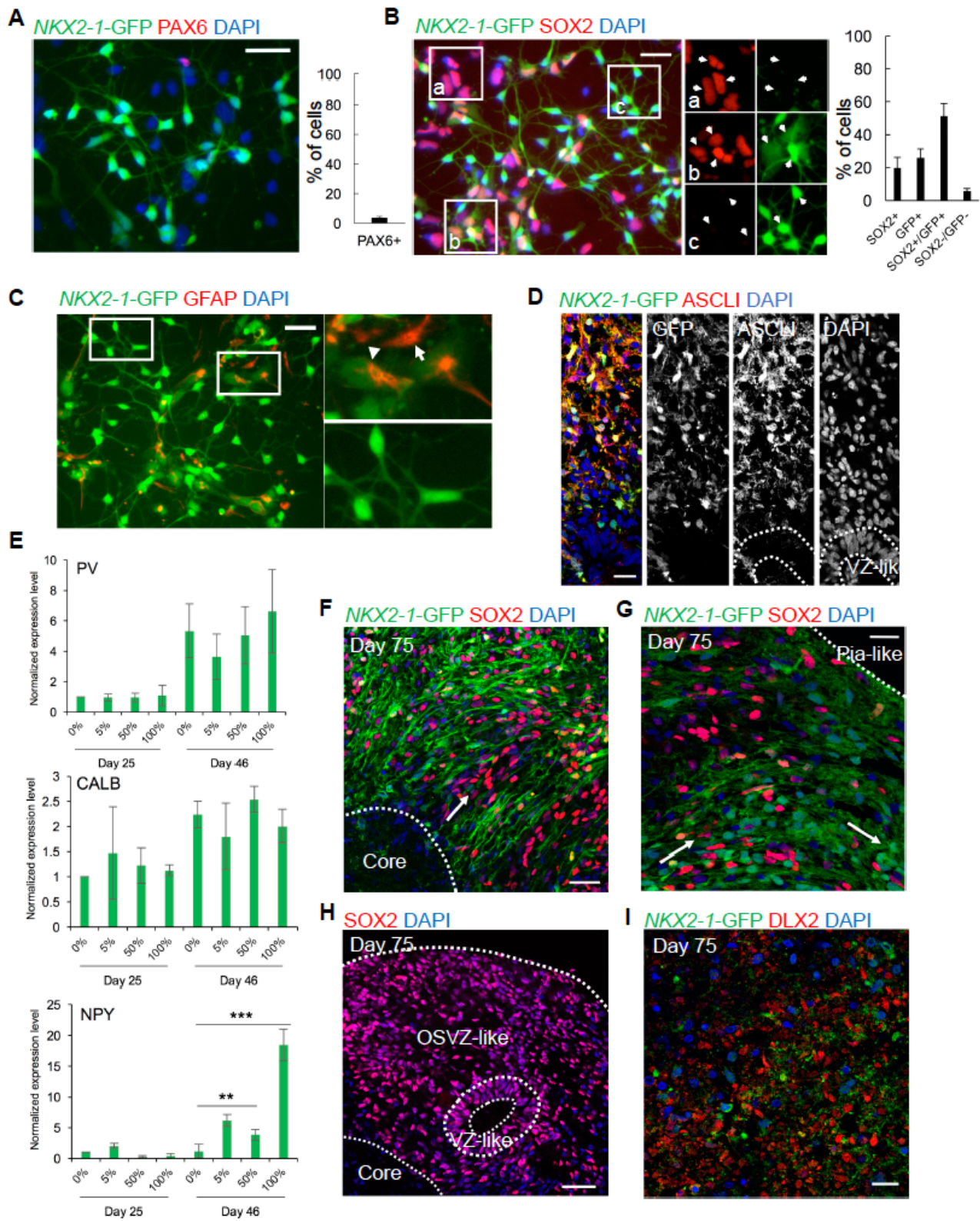


Figure S2

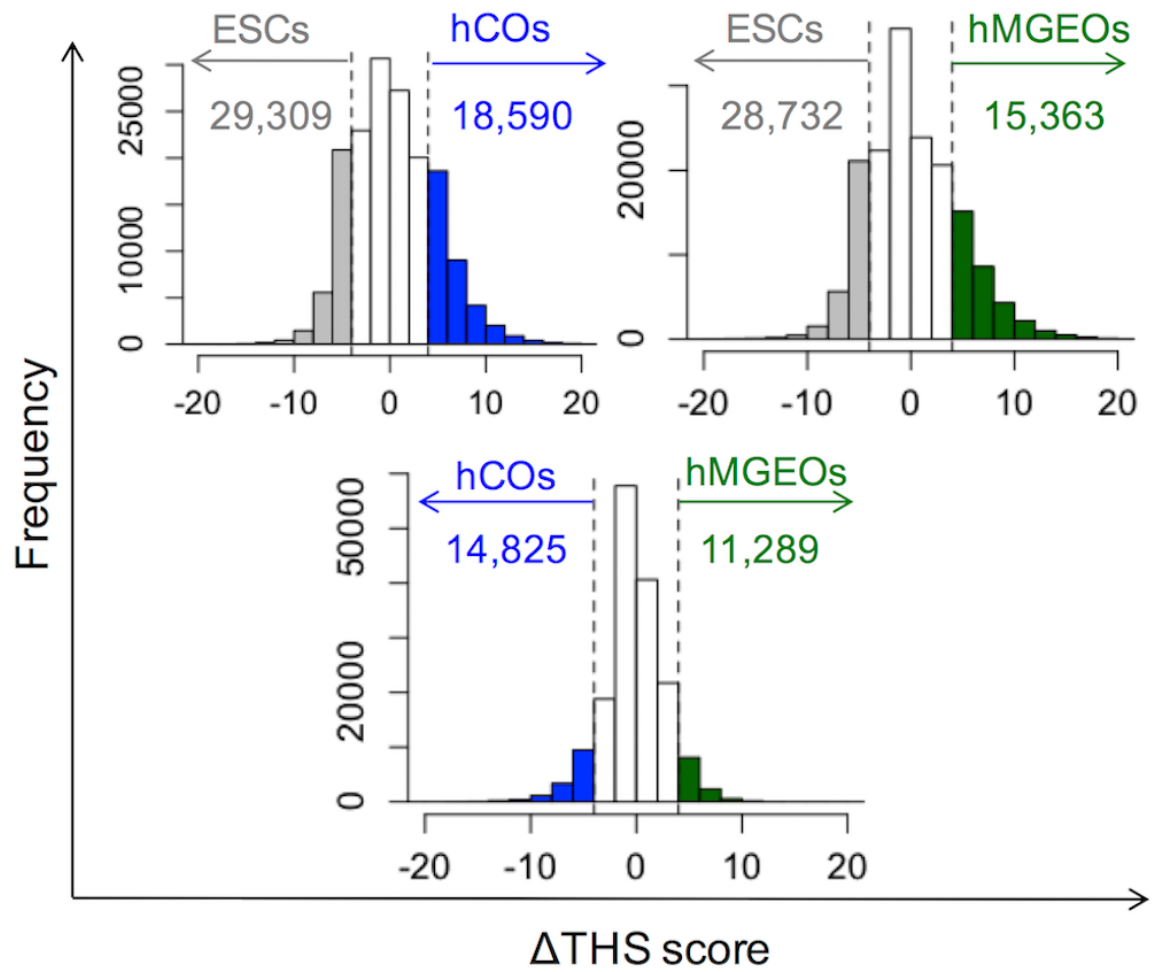
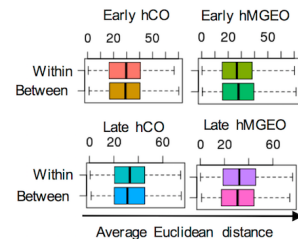


Figure S3

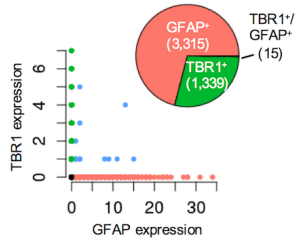
A

Name	Estimated Number of Cells	Median Mean Reads per Cell	Genes per Cell	Number of Reads	Total Genes Detected	Median UMI Counts per Cell
early hCO rep1	6,480	21,437	1,582	138,912,573	20,421	4,475
early hCO rep2	10,258	13,206	1,212	135,471,888	20,380	2,626
early hMGE rep1	2,969	47,466	1,756	140,927,324	19,564	4,845
early hMGE rep2	9,722	14,392	1,306	139,928,458	20,177	2,864
late hCO rep1	6,355	21,397	1,319	135,979,670	21,705	2,589
late hCO rep2	9,193	14,930	1,876	137,257,722	23,343	4,305
late hMGE rep1	5,438	23,487	1,557	127,722,890	21,664	2,985
late hMGE rep2	8,820	16,782	1,962	148,039,404	23,377	4,542

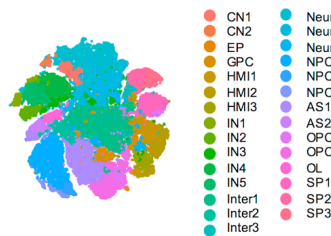
B



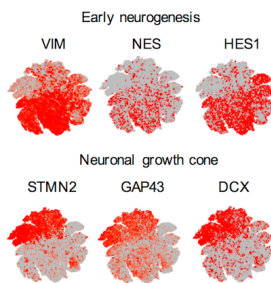
C



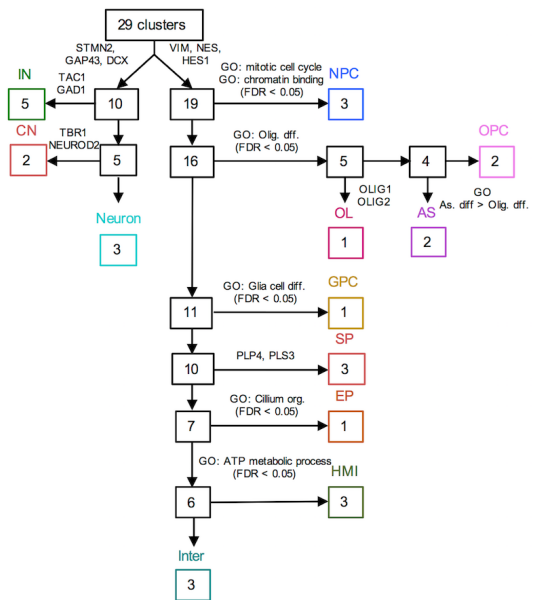
D



F



G



E

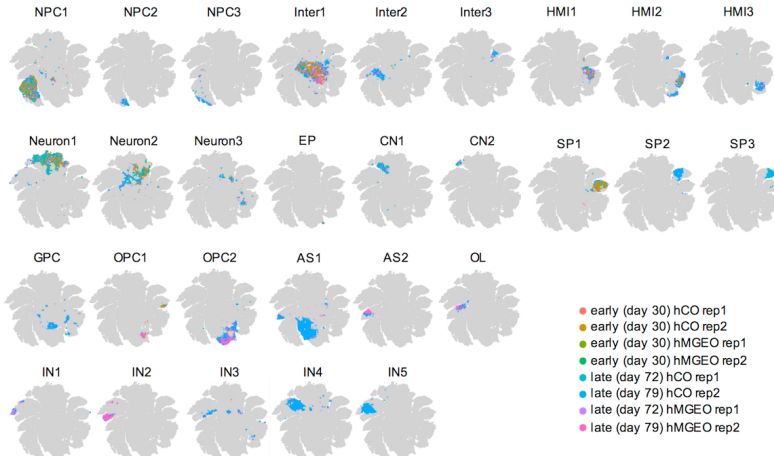


Figure S4

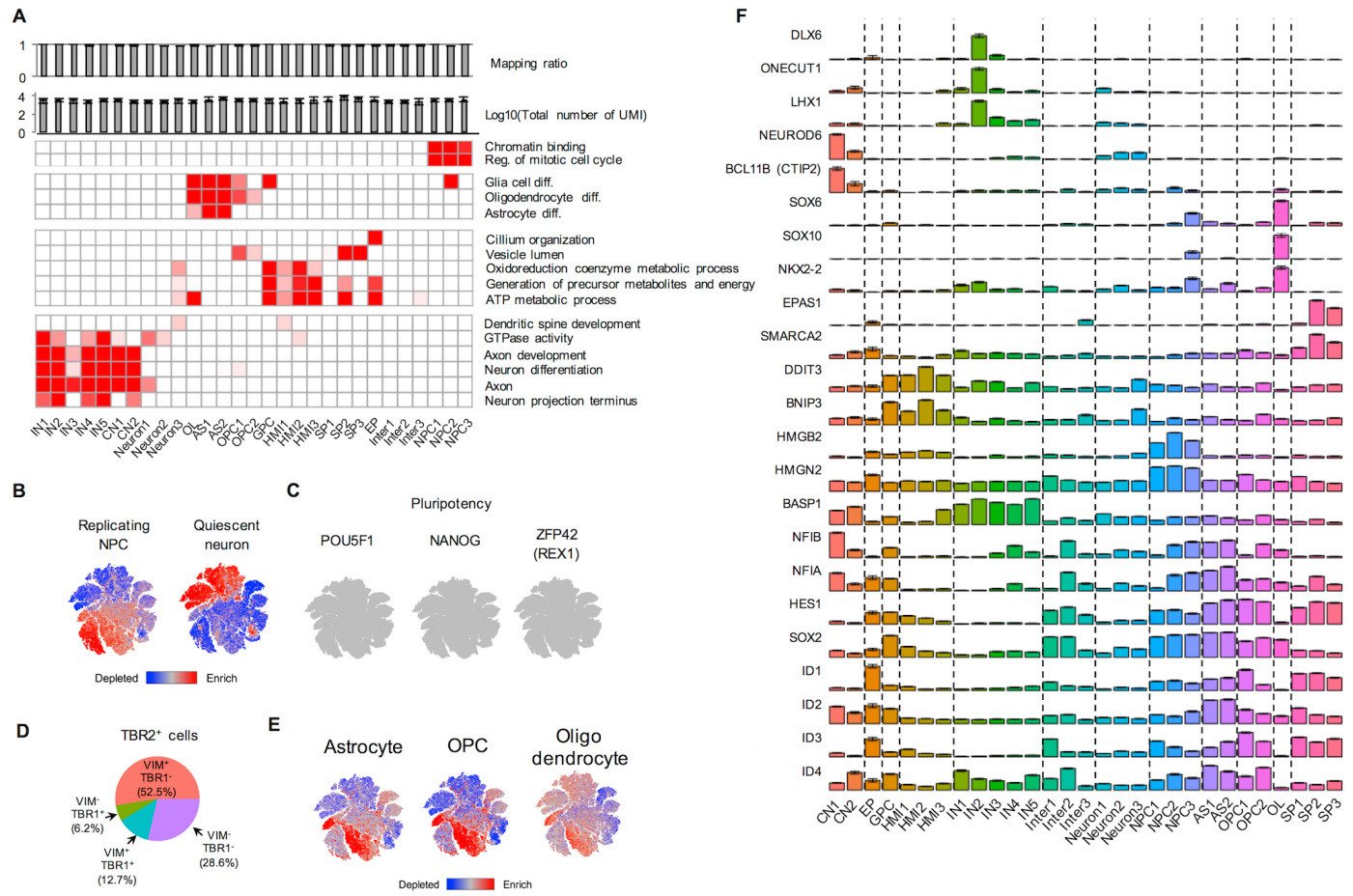


Figure S5

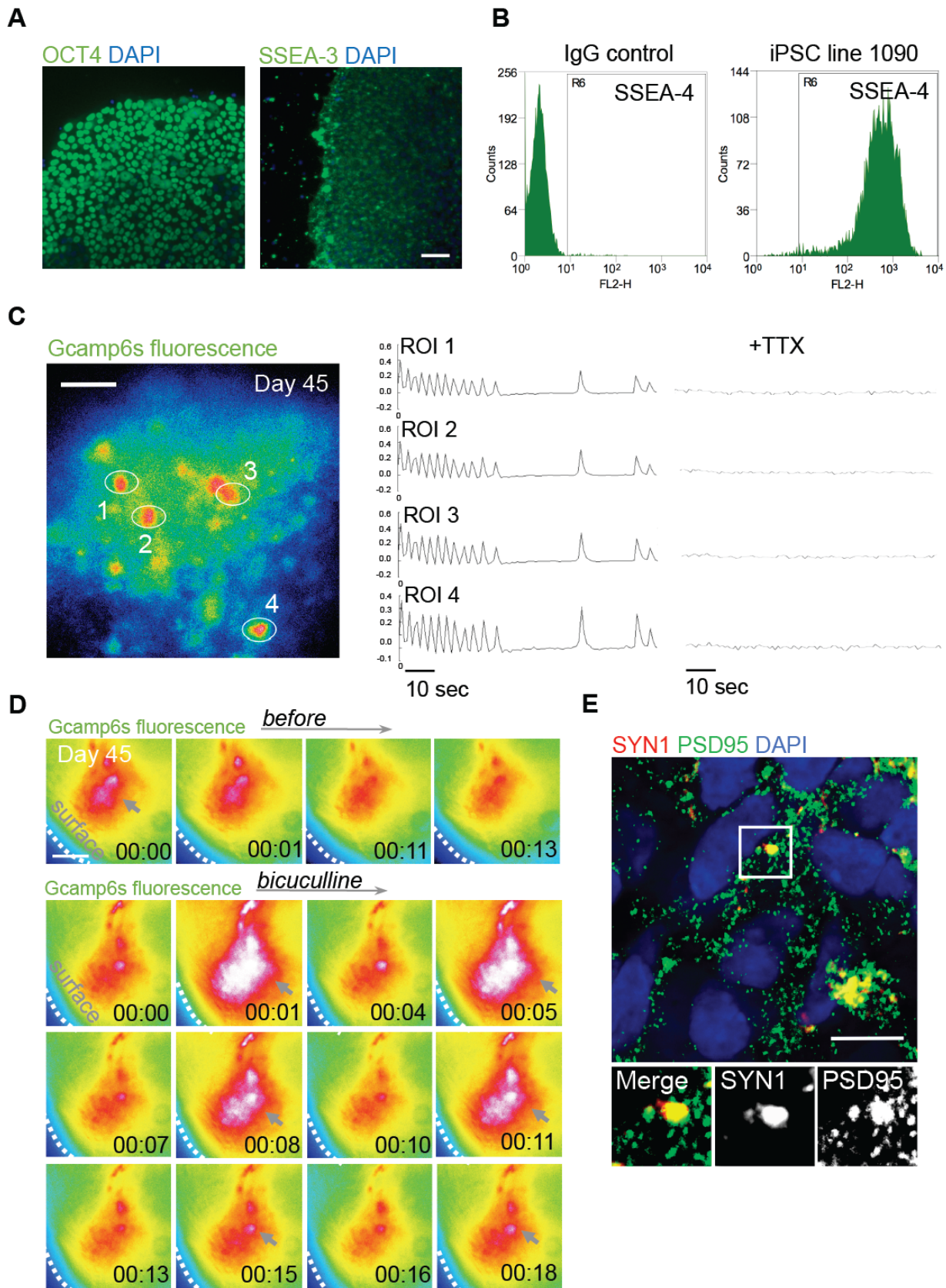


Figure S6

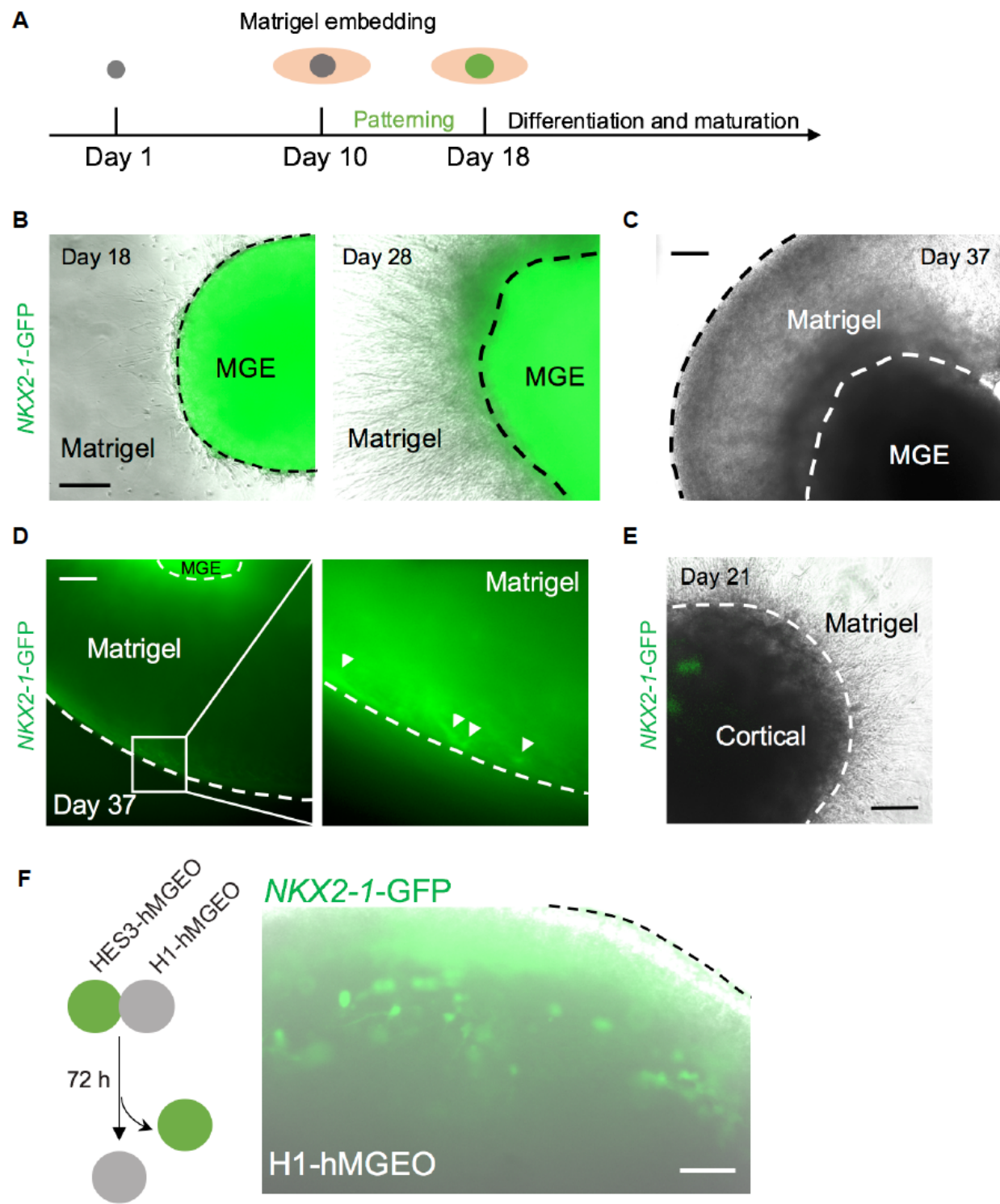
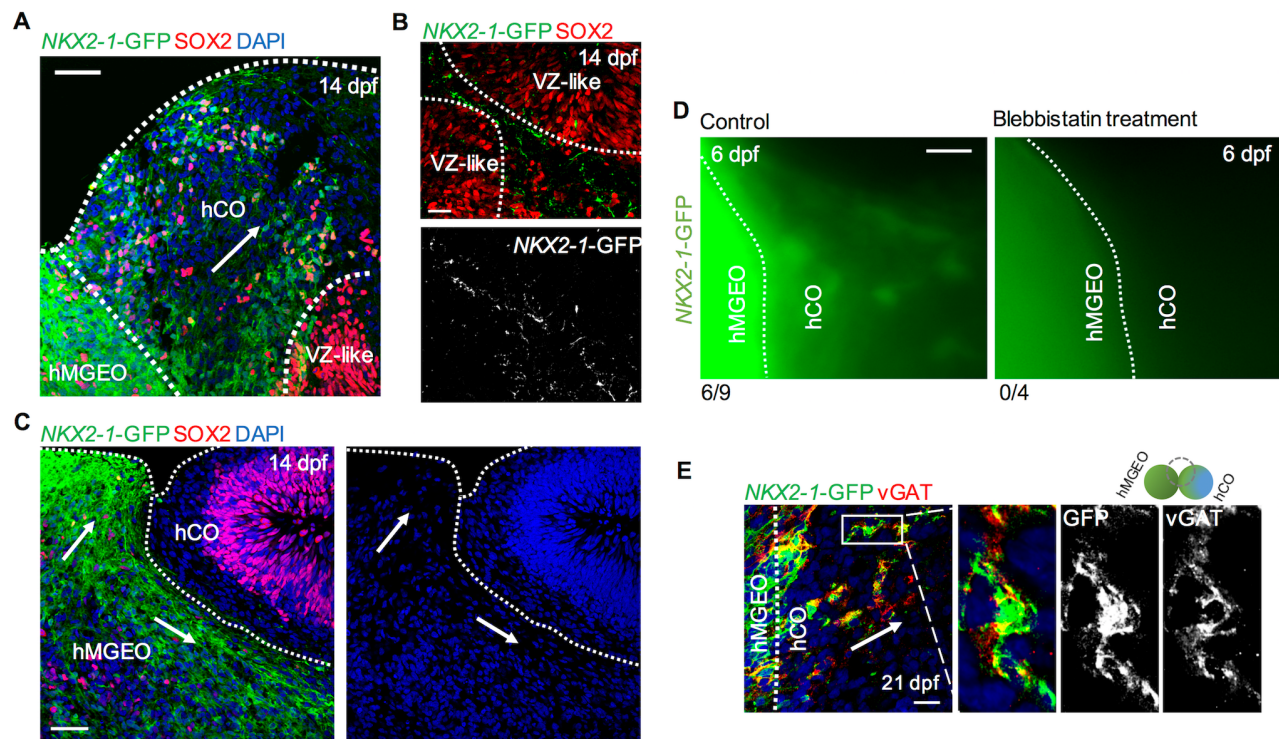


Figure S7



Supplemental Movies

Movie S1: Calcium surges of neurons inside hMGEOs

Movie S2: Calcium surges of neurons inside hCOs without Bic treatment

Movie S3: Calcium surges of neurons inside hCOs with Bic treatment

Movie S4: Live imaging of neuron migration side hfMCOs

Movie S5: Live imaging of neuron migration side hfMCOs without Blebbistatin treatment

Movie S6: Live imaging of neuron migration side hfMCOs with Blebbistatin treatment